Journal Pre-proofs

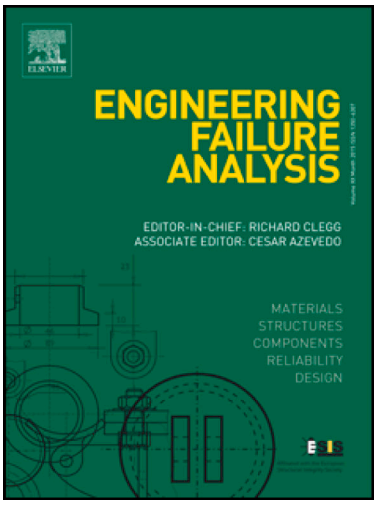

Macroscale modelling of the orthotropic shear damage in the dynamics of masonry towers by RBSM

Siro Casolo

PII: S1350-6307(21)00605-1
DOI: https://doi.org/10.1016/j.engfailanal.2021.105744
Reference: EFA 105744

To appear in: *Engineering Failure Analysis*

Received Date: 7 April 2021
Revised Date: 12 September 2021
Accepted Date: 12 September 2021

Please cite this article as: Casolo, S., Macroscale modelling of the orthotropic shear damage in the dynamics of masonry towers by RBSM, *Engineering Failure Analysis* (2021), doi: https://doi.org/10.1016/j.engfailanal.2021.105744

- Unique orthotropic shear response of the masonry can be accounted by a rigid body-spring model;
- Different shear strength and internal friction, parallel and normal to the plane of the bed;
- Comparison of these different constitutive assumptions to explain of a vertical pattern of cracks along masonry towers;
- Numerical analyses show a better capability to predict the crack pattern of an idealized tower

Declaration of interests

X The authors declare that they have no known competing financial interests or personal relationships that could have appeared to influence the work reported in this paper.

☐The authors declare the following financial interests/personal relationships which may be considered as potential competing interests:

Macroscale modelling of the orthotropic shear damage in the dynamics of masonry towers by RBSM

Siro Casolo[a,*]

[a]*Department ABC, Politecnico di Milano, Italy*

Abstract

The peculiarity of a rigid body-spring model (RBSM) is exploited to predict and explain a specific damage pattern and failure that is often observed in ancient masonry towers subjected to seismic events. In fact, the full understanding of the frequent appearence of a vertical pattern of cracks along the height of these buildings, which could be viewed as a macroscopic mode II shear fracture, would require to overcome the macroscopic approach based on the standard Cauchy solid continuum. The research focuses on the orthotropic shear response of the masonry material, related to its bond/texture pattern, which is here accounted by a RBSM that allows to assign, heuristically, a different shear strength and internal friction, parallel and normal to the plane of the mortar bed joints. This specific feature, in the context of a set of full dynamical analyses, appears to be a key to predict the crack pattern and failure of an idealized masonry tower, in accordance with the surveys of real towers subjected to strong ground motions.

Key words: Rigid Body Spring Model, Dynamics, Orthotropy, Shear damage, Failure, Masonry, Tower

1. Introduction

The structural analysis of large masonry structures requires a macro-scale modelling, that avoids the explicit representation of the meso-scale internal structure of the material. The overall mechanical response of a fairly well-organized masonry material is related to the bond/texture arrangement which is qualitatively characterized by two main aspects: (i) the shape and the bond/texture arrangement of the brick/blocks strongly determine the crack pattern development; (ii) the common pratice of masonry construction is based on the creation of quite regular horizontal mortar layers, while the vertical mortar joints are staggered.

*Corresponding author, e-mail: siro.casolo@polimi.it

Depending on the emphasis given to the different aspects of the macroscopic response, some specific areas in the field of computational masonry mechanics have been cultivated by the scientific community. A main research line concerns the definition of macroscopic models with orthotropic characteristics which should be derived from the effective bond/texture geometry at the meso-scale. In this case, the macro-scale response can be based on refined models with an explicit meso-scale description of the geometric arrangement of the blocks, or with a detailed behaviour of the mortar joints and interfaces at the micro-scale [1, 2]. Several homogenization techniques, including multiscale, have been elaborated to accomplish the scale transition and most of these studies aims to implement numerical precedures adopting finite element approaches based on the Cauchy solid continuum model [3–10]. In theory, within the framework of continuum solid mechanics, the masonry modelling takes benefit of an enriched kinematics, e.g. by exploiting the peculiarities of the Cosserat micropolar theory [11–13], which also allows to account for the size effect and the implicit non-local behaviour that depends on the shape and the stiffness of the blocks [14–18]. Unfortunately, in the effective adoption of these refined computational models becomes problematic when the overall mechanical response should be evaluated under dynamical conditions in which the material develops damage and fractures, as is the case of buildings subjected to seismic loadings.

A fairly different paradigm is associated to the models based on a fully discrete approach [19, 20]. These models are largely driven by the objective of predicting the damage and post-failure behaviour of fragile and/or heterogeneous materials, and are boosted by the great development of computer processing power. Thus, various discrete methods have been proposed for structural mechanics applications, based on a mainly mechanistic approach, or by a more general and fundamental theoretical vision. Among these, the spring network models or the lattice models, in which the solid is imagined as an assembly of masses connected by springs, or as a grid of beams, as well as the numerical models arising from peridynamics theory, that have proved very effective [21–26].

Focusing to the macroscale analysis of a masonry material, a specific Rigid Body and Spring Model (RBSM [27]) was proposed by the author for the description of the non-linear in-plane response of the masonry material. This model has been implemented to manage the macroscale shear damages that arise from three empirical and computational evidences related to the geometric arrangement of the brick/blocks [28]: (i) the brick/block aspect ratio determines the macroscopic crack pattern; (ii) for low values of vertical compression loads, the shear slidings tend to propagate quite easily along the horizontal mortar layers,

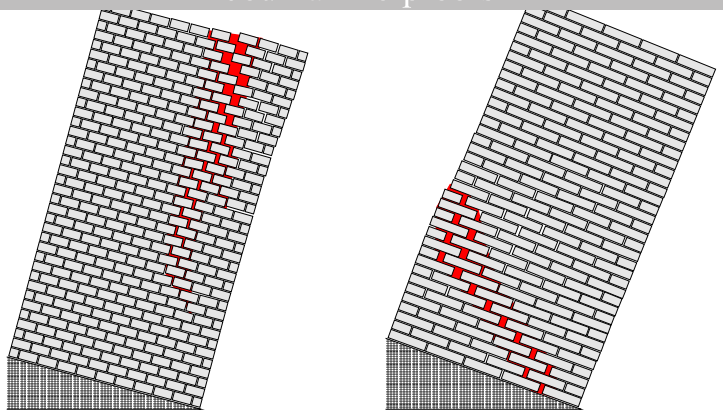

Figure 1: Crack patterns of walls made by dry blocks on inclined planes. Header bond on the left side, stretcher bond on the right. These heuristic sketches are based on the pictures published in [29].

while the macroscopic *mode II* propagation along the vertical direction is contrasted by the staggered brick/block disposition; (iii) in the case of high levels of vertical compression load, the internal friction significantly enhances the shear strength of the horizontal mortar joints while this effect is substantially irrelevant for the vertical joints.

The prevalence of a single or of a combination of these behaviours depends to a large extent on the specific geometry of the masonry wall, as highlighted, for example, by Giuffré on the basis of a set of simple laboratory experiments on walls assembled with dry blocks of different aspect ratios [29], and recently by Baraldi et al. [30] by means of a computational approach that highlighted the effects of the micro-structure. Figure 1 shows a couple of heuristic sketches that summarize two Giuffré's experiments in which the base of the specimens was progressively inclined until the development of a global collapse kinematics. In the left side wall, the low aspect ratio of the blocks implied a weak interlocking, which offered a scarce contrast to the early slipping of the dry blocks in the upper area, where the low vertical load did not guarantee an effective friction along the horizontal interfaces. Thus, the macroscopic collapse mechanism consisted in the opening and widening of a vertical crack that developed top-down and disgregates the masonry. The stretcher bond, on the right side wall, guaranteed a better interlocking which prevented the previous early mechanism and allowed the wall to resist until the reaching of an angle of inclination about 1/3 larger. The final collapse, thus, was a combination of a global rotation associated with the sliding of the horizontal joints in the lower part of the wall. The role of the different interlocking provided by the two wall bond-textures, in combinaton with the internal friction, is evident.

For tall buildings, such as the masonry towers, however, the situation is more complex

and difficult to interpret, especially in the case of seismic loads. In fact, the vertical compression stress due to the gravity load gives a quite good resistence to the sliding of the horizontal joints throughout the lower part of these buildings. On the other hand, during a seismic time history, the shear stress at the centre of the façades can be relevant also in the upper part, because of the effect of the higher-order natural modes of vibration, while the shear strength is only slightly affected by the low value of vertical compression stress. In addition to this, the situation is further complicated by the fact that the variation of the bending moment due to the seismic loads causes a variation in the effects of the internal friction which can locally reduce the shear resistance of the horizontal joints. Ultimately, it can happen that the shear stress can overcome alternatively the macroscopic cohesion related to the bond-texture interlocking, and/or the strength related to the internal friction, prompting damage scenarios that are difficult to predict without an appropriate dynamical analysis.

In the following Section 2, some experimental and numerical data are recalled, in order to give a base on which defining the numerical parameters of a model to account for the orthotropy of the macroscopic shear behaviour. Then, in Sections 3 and 4, it will be shown how an orthotropic shear response is obtained by means of the RBSM approach, while Section 5 presents the new application of the model, focusing on the peculiarity that this RBSM model allows to compare the different damage patterns related to the different shear constitutive assumptions. The discussion is based on a preliminar pushover analysis, and above all on a set of dynamical seismic simulations.

Nomenclature

a	exponent that determines the degradation of the unloading stiffness
a_x^{ij}, a_y^{ij}	axial spring-bonds that connects elements i, j along x, y axes
b_x, b_y	distance of the axial springs-bonds from the midpoint of the elements side
$[B]$	strain-displacement matrix
$[C]$	viscous damping matrix
h_x, h_y	distance of the element centroid from the side, along x, y direction
d_i	distance of the i-element centroid from the midpoint of the connection side
$[D_t]$	local-bond tangent stiffness matrix
E	Young's modulus
$E_{\alpha\beta}$	component of the plane strain tensor
$\{f^0\}$	vector of generalised forces

G	shear modulus
$G_h^{f\text{II}}, G_v^{f\text{II}}$	mode II fracture energy along horizontal and vertical directions
k^A, k^S	stiffness of the axial and shear spring-bonds
$[K_t]$	generalised tangent stiffness matrix
m	number of rigid elements of the problem
m_i	mass of $i-$element
ι_i	polar moment of $i-$element
$[M]$	mass matrix
$\tilde{n}$	normal versor
s_x^{ij}, s_y^{ij}	shear spring-bonds that connects elements i, j along x, y axes
$\tilde{t}$	tangent versor
x^i, y^i	co-ordinates of the centroid of i-element
u^i, v^i	displacement components of the centroid of i-element, along x, y
$\{u\}$	vector of generalized displacements
$[V]$	matrix of volumes of pertinence
$[X]$	configuration matrix with the centroids co-ordinates
α	angle between the edge of an element and the x-axis
β	factor that determines the distance b
β_N, ϵ_N	parameters of Newmark's time step integration scheme
ε	measure of strain in a spring-bond
$\{\varepsilon\}$	vector of generalised strain
γ	shear strain
μ	internal friction coefficient
σ	axial force per unit of area
τ	shear force per unit of area
θ	angle between the normal to the connection side and the $x-$axis
ϕ^i	angle of orientation of the rigid i-element
$[\Phi]$	configuration matrix with the orientations of all the rigid elements
ψ^i	variation of angle of rotation of the i-element
ω^i	rigid i-element

2. Anistropic shear response of masonry panels

Qualitativey, the anisotropy in the shear fracture process of a masonry wall built according with a regular bond-texture is quite obvious. At the micro-scale, the response of the horizontal mortar joints subjected to shear loading has been deeply investigated, and the role of the internal friction on the post-elastic behaviour is well acknowledged [31–34]. A number of experiments have shown how the mode II fracture energy $G^{f\mathrm{II}}$ increases with the compressive stress, and a linear correlation can be reasonably assumed. On the other hand, the development of a vertical crack pattern is the result of a more complex behaviour because the opening/sliding along the vertical staggered joints is affected by the arrangement of the blocks that interrupt the joints continuity. The macro-scale shear response and failure is usually handled in the frame of continuum mechanics by numerical approaches inspired by the classic models of Mohr-Coulomb or Drucker, and a certain degree of orthotropy can be introduced in accordance with the natural axes of the masonry bond/texture [35–40]. The parameters to be assigned to these numerical models can be defined by means of computational homogenization techniques, which generally assume regular bond-texture arrangement, while the classic diagonal compression test, that was conceived originally to evaluate the tensile strength of isotropic materials, is also sometimes considered as a support to the experimentation.

Clearly, the damage-induced anisotropy effect finds its origin in the meso-structure of the material [41]. An interesting attempt to highlight experimentally the different shear fracture strengths, i.e. the strength dependence on the orientation of the shearing fracture plane, parallel or orthogonal to the horizontal mortar joints, can be found in a quite little-known paper by Malyszko [42] in which the loading scheme was conceived in order to obtain the shear loading at the specimen's midlength by the application of two counteracting forces according with a configuration that can be traced back to the Iosipescu method [43]. Recently, an experimental campaign has also been conducted at the Politecnico di Milano laboratories, with the aim of characterizing the different shearing fracture modes by means of tests on masonry panels with the load configuration shown in the Figure 2 [44]. These experiments showed a clear difference in the values of shear resistence, with the collapse load obtained with a shear fracture propagating normal to the bed joints that was always higher than the case in which the fracture develops along the horizontal joints.

Heuristically, it is clear that a possible fracture due to the shear sliding tends to

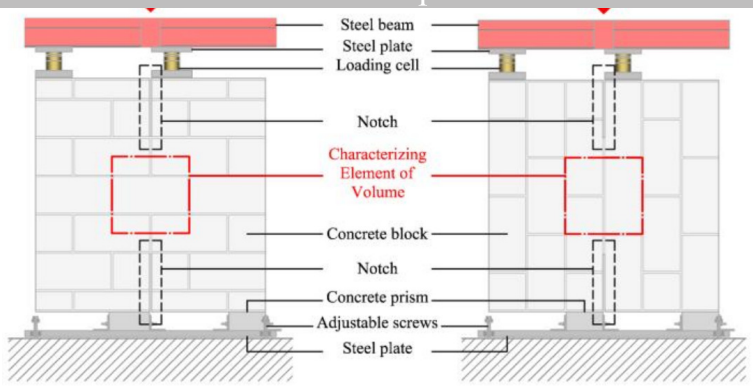

Figure 2: Loading configuration: shear crack normal to bed joint (on the left), and shear crack parallel to bed joint (on the right) [44].

propagate quite easily along the horizontal mortar joints since they are continuous, while vice versa, the shear crack propagation along a vertical joint is hampered by the presence of the blocks that interrupt its continuity. This becomes macroscopically evident in a deep beam loading scheme, when the texture of a masonry is rotated through 90^o [28]. This notwitstanding, the determination, by experiments as well as by numerical analysis, of the parameters needed to describe quantitatively these aspects presents considerable difficulties, both practical and theoretical, also due to the typological variability of the heterogeneous material. Quite different strength values and a different toughness of the macroscopic development of the shear fracture pattern can be often observed in realistic masonries.

Experimental tests have shown how important it is to take into account the orientation of principal axes of the texture with respect to the applied stress [45], and various combination of in plane actions produce very different mechanisms, [46]. To date, a shared procedure has not been established to quantify experimentally or numerically the orthotropy of the shear strength response. From the classic shear tests of Atkinson et al. [47] a good accordance with the Coulomb criterion based on cohesion and friction has been always accepted. Thus, several authors have introduced a Coulomb friction law for plasticity models when modelling masonry [3, 48], and in the case of cyclic loading, usually it is also considered that a residual resistance of friction type tends to persist [49, 50]. In any case, this research is oriented towards a theoretical and computational character, even if it takes its cue from the observation of some empirical aspects that characterize the mechanical response of masonry towers.

3. The rigid body and spring model for masonry material

3.1. Discretization and kinematics

The masonry material is here discretized at the macro-scale by a specific Rigid Body-Spring Model (RBSM) that consists of an assemblage of m rigid elements connected by elastic-plastic spring-bonds. The basic concept of this approach is that the main macroscopic mechanical characteristics of the heterogeneous masonry can be resumed by an *heuristic-molecule* [12, 20] composed of 4 rigid masses connected by line-springs arranged so as to give axial, shear, and in-plane flexural bonding actions, as shown in Fig. 3. The grey shaded quadrilateral is the area that corresponds to the unit cell, or heuristic-molecule, whose vertex are the centroids of the four rigid masses, or elements, linked by the axial spring-bonds $\{a_{12}, a_{23}, a_{34}, a_{41}\}$, and the shear spring-bonds $\{s_{12}, s_{23}, s_{34}, s_{41}\}$. The geometric configuation is fully defined by the co-ordinates $\{x^i, y^i\}_{i=1,m}$ and the angle of orientation ϕ^i around the centroid of each element ω^i, with $i = 1, \dots m$. A varied configuration, indicated by symbol $\star$, is defined as a function of the displacements: $u^i = x^{\star i} - x^i$, $v^i = y^{\star i} - y^i$, $\psi^i = \phi^{\star i} - \phi^i$. These $3m$ variables are assembled into the vector of Lagrangian coordinates, as follows:

$$\{u\}^T = \left\{u^1, v^1, \psi^1, u^2, v^2, \psi^2, \dots, u^m, v^m, \psi^m\right\} \tag{1}$$

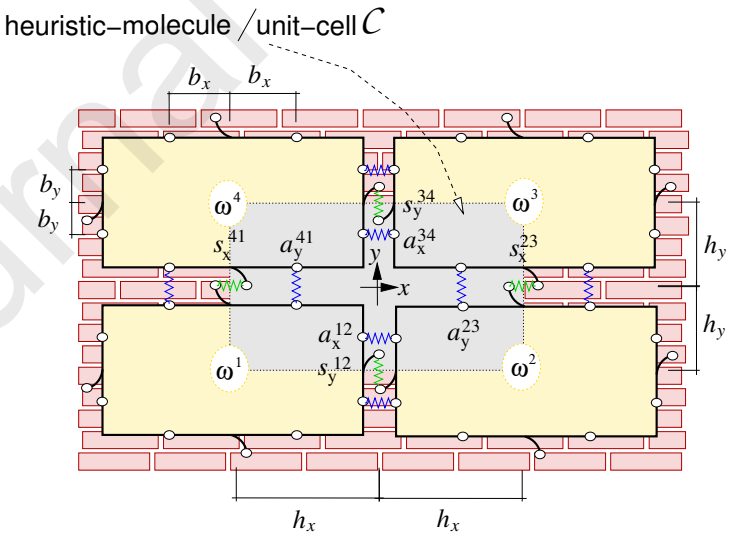

Figure 3: Heuristic representation of a unit cell made of rigid masses and springs. Differently from the drawing, the mathematics refers to an initial lenght of the spring that is null.

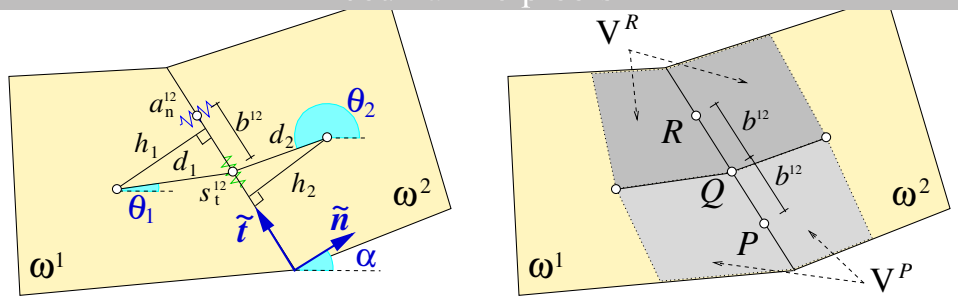

Figure 4: Couple of rigid elements ω^1 and ω^2 of irregular shape with evidence of the notation adopted.

145 The elastic forces are related to the change of distance of the points, connected by the springs, that are initially superposed. [1]

For the case of a discretization based on rectangular unit cells, Fig. 3, the macroscopic bond elongations Δa_n^{ij} and Δs_t^{ij} can be put in relation with the measures of strain $E_{\alpha\beta}$ of a plane Cosserat-like solid. To show this, making reference to the quarter of the grey unit cell that belongs to the regular element ω^1, with the sides aligned with the axes x, y, the following limit can be roughly considered:

$$\lim_{\substack{h_x\to 0\\ h_y\to 0}} \begin{bmatrix} \Delta a_x^{12}/2h_x & \Delta s_x^{41}/2h_y \\ -\Delta s_y^{12}/2h_x & \Delta a_y^{41}/2h_y \end{bmatrix} = \begin{bmatrix} u^1_{,x} & u^1_{,y}+\psi^1 \\ v^1_{,x}-\psi^1 & v^1_{,y} \end{bmatrix} = \begin{bmatrix} E_{xx} & E_{xy} \\ E_{yx} & E_{yy} \end{bmatrix} \tag{2}$$

So, even if in an approximate way, this discrete model has the ability to describe an enriched kinematics with regard to shear behaviour. Now, to examine the behaviour of a more realistic large-scale structure, the case of distorted discretization should also be handled. With reference to a case of a unit cell assembled with distorted quadrilateral elements, Fig. 4 shows the connection between the couple ω^1-ω^2. The variation of lenght of the axial bond, Δa_n^{12}, and of the shear bond, Δs_t^{12}, when considering a linearized

[1] The representation given in Fig. 3 only has an evocative/heuristic value, since the model does not have compenetrations or separations of matter. Moreover, under the hypothesis of small displacements and rotations, only the component of elongation normal Δa_n^{ij}, or parallel Δs_t^{ij}, to the connection side are considered, respectively for the axial or shear bond/springs.

kinematics for small displacements, are expressed by:

$$\left\{ \begin{array}{c} \Delta a_n^{12} \\ \Delta s_t^{12} \end{array} \right\} = - \left[\begin{array}{ccc} \cos\alpha & \sin\alpha & [d_1 \sin(\alpha-\theta_1) - b^{12}] \\ \sin\alpha & -\cos\alpha & [-d_1 \cos(\alpha-\theta_1)] \end{array} \right] \left\{ \begin{array}{c} u^1 \\ v^1 \\ \psi^1 \end{array} \right\} + \left[\begin{array}{ccc} \cos\alpha & \sin\alpha & [\, d_2 \sin(\alpha-\theta_2) - b^{12}] \\ \sin\alpha & -\cos\alpha & [\, d_2 \cos(\alpha-\theta_2)] \end{array} \right] \left\{ \begin{array}{c} u^2 \\ v^2 \\ \psi^2 \end{array} \right\} \tag{3}$$

Then, two corresponding discrete measures of strain can be estimated by the ratios:

$$\varepsilon_n^{12} = \Delta a_n^{12}/(h_1+h_2) \qquad\qquad \varepsilon_t^{12} = \Delta s_t^{12}/(h_1+h_2) \tag{4}$$

The deformation of the whole discrete model is thus accounted by collecting three strain measures in correspondence of the points P, Q and R, placed along the common side as shown in Fig. 4, for each couple of adjoining mass-elements. These measures are associated with the volumes of pertinence V^P and V^R for the axial bonds, and $\mathrm{V}^Q = \mathrm{V}^P + \mathrm{V}^R$ for the shear bond. Considering a discrete model with r sides that connect all the elements, the vector of generalised strain $\{\varepsilon\}$ and the diagonal matrix of volumes of pertinence $[V]$ are defined as follows:

$$\{\varepsilon\}^T = \left\{ \varepsilon_1^P, \varepsilon_1^Q, \varepsilon_1^R, \varepsilon_2^P, \varepsilon_2^Q, \varepsilon_2^R, \ldots, \varepsilon_r^P, \varepsilon_r^Q, \varepsilon_r^R \right\} \tag{5}$$

$$[V] = \mathrm{Diag} \left\{ \mathrm{V}_1^P, \mathrm{V}_1^Q, \mathrm{V}_1^R, \mathrm{V}_2^P, \mathrm{V}_2^Q, \mathrm{V}_2^R, \ldots, \mathrm{V}_r^P, \mathrm{V}_r^Q, \mathrm{V}_r^R \right\} \tag{6}$$

According with the expressions given by Eqs. (3- 4), the strain-displacement relations can be expressed by assembling a $3r \times 3m$ matrix $[B]$ as follows:

$$\{\varepsilon\} = [B]\{u\} \tag{7}$$

3.2. Equations of the motion

The measure of stress, conjugated in virtual work with the strain associated to each bond, is given according with an incremental formulation $\{\sigma\} = \{\sigma^0\} + \{\Delta\sigma\}$ so that the internal virtual work done by the elastic-plastic springs is:

$$\begin{aligned} \delta\mathcal{W}^i &= \{\delta\varepsilon\}^T [V]\{\sigma^0\} + \{\delta\varepsilon\}^T [V][D_t]\{\Delta\varepsilon\} = \\ &= \{\delta u\}^T \left(\{f^0\} + [K_t]\{\Delta u\} \right) \end{aligned} \tag{8}$$

where vector $\{\Delta\varepsilon\}$ collects the strain increments, and $[D_t]$ is the "local-bond" tangent stiffness matrix :

$$[D_t] = \text{Diag}\left\{k_1^P, k_1^Q, k_1^R, k_2^P, k_2^Q, k_2^R, \ldots, k_r^P, k_r^Q, k_r^R\right\} \tag{9}$$

The vector of generalised forces $\{f^0\}$, and the generalised tangent stiffness matrix$[K_t]$ are:

$$\begin{aligned} \{f^0\}^T = &\ \{\sigma^0\}^T[V][B] \\ [K_t] = &\ [B]^T[V][D_t][B] \end{aligned} \tag{10}$$

The absolute kinetic energy of the whole discrete system depends on the time derivative of the total displacements, sum of those relative to the base $\{\dot{u}\}$ plus the ground motion due to the seismic action $\{\dot{u}_g\}$:

$$\mathcal{T}_f^e = \frac{1}{2}(\{\dot{u}\} + \{\dot{u}_g\})^T\ [M]\ (\{\dot{u}\} + \{\dot{u}_g\}) \tag{11}$$

where the diagonal generalised mass matrix collects the mass of each element m_i and the polar moment of inertia ι_i

$$[M] = \text{Diag}\left\{m_1, m_1, \iota_1, m_2, m_2, \iota_2, \ldots, m_m, m_m, \iota_m\right\} \tag{12}$$

Thus, the first variation of the absolute kinetic energy with respect to an arbitrary variation of the Lagrangian coordinates $\{\delta u\}$ is [51]:

$$\delta\mathcal{T} = -\left([M]\{\ddot{u}\} + [M]\{\ddot{u}_g\}\right)^T\{\delta u\} \tag{13}$$

A viscous matrix $[C]$, proportional to the mass matrix $[C] = a_0[M]$, is assumed to model the energy dissipation for very small deformations, that does not involve any damage. The parameter a_0 is assigned in order to obtain a prescribed value of damping relative to the first natural mode of vibrating. Thus, the virtual work of these viscous forces for the whole system is

$$\delta\mathcal{W}^d = -\left([C]\{\dot{u}\}\right)^T\{\delta u\} \tag{14}$$

The higher modes are damped by adopting a numerical dissipation, which in this specific case consists of assigning the values $\beta_N = 0.4225$ and $\epsilon_N = 0.8$ to the parameters of Newmark's time step integration scheme [52].

Then, by applying the fundamental theorem of the calculus of variations, the Euler-Lagrange equations that govern the motion of the model during each integration time step are obtained:

$$[M]\{\ddot{u}\} + [C]\{\dot{u}\} + \{f^0\} + [K_t]\{\Delta u\} = -[M]\{\ddot{u}_g\} \tag{15}$$

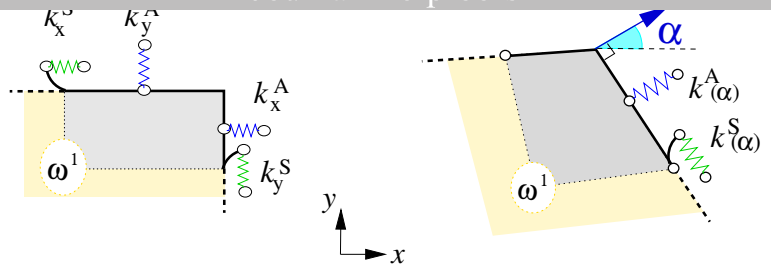

Figure 5: Heuristic representation of a quarter of unit cell made of rigid masses and springs.

The time integration is performed through the implicit Newmark scheme. At each time step, this is solved adopting the full Newton-Raphson iteration scheme until numerical convergence is attained [52].

3.3. Parameters for the elastic response

The elastic characteristics of the spring-bonds are defined on each quarter of element, to which 4 connecting devices are attached. With reference to the regular quarter of element ω_1 shown in grey colour in Fig. 5 (left side), the four associated stiffnesses are indicated by k_x^a, k_y^a, k_x^s, k_y^s, and are defined by balancing the elastic energy of 3 different deformed conditions of the discrete assemblage with the elastic energy of the unit-cell made by a corresponding orthotropic continuum [2] [12]. These values are then modified when adopting distorted elements accordingly to what explained in a previous paper [53]. This aspect, in the present application, has little relevance because the elements of the mesh adopted are generally almost rectangular with the sides aligned with the material reference axes. Moreover, the discretization is at a scale quite coarser than the individual blocks size, and thus, according with [53], the proposed model does not need to apply a specific strategy to account for the flexural in-plane interlocking effects of these elements.

[2] Given the elastic moduli $\mathsf{C}_{\alpha\beta\delta\gamma}$ and $\mathsf{D}_{3\alpha3\alpha}$ of an orthotropic Cosserat continuum, the corresponding spring-bond stiffnesses of a RBSM which disregards the Poisson's effects can be obtained by:

$$\begin{aligned} k_x^A &= \frac{\mathsf{C}_{1111}\mathsf{C}_{2222}-\mathsf{C}_{1122}^2}{\mathsf{C}_{2222}} & \qquad k_x^S &= \frac{\mathsf{C}_{1212}\mathsf{C}_{2121}-\mathsf{C}_{1221}^2}{\mathsf{C}_{2121}-\mathsf{C}_{1221}} \\ k_y^A &= \frac{\mathsf{C}_{1111}\mathsf{C}_{2222}-\mathsf{C}_{1122}^2}{\mathsf{C}_{1111}} & \qquad k_y^S &= \frac{\mathsf{C}_{1212}\mathsf{C}_{2121}-\mathsf{C}_{1221}^2}{\mathsf{C}_{1212}-\mathsf{C}_{1221}} \end{aligned} \tag{16}$$

while, the distances b_x and b_y can be obtained as a function of in-plane Cosserat flexural stiffnesses:

$$b_x = \beta_x h_x = \sqrt{\frac{\mathsf{D}_{3131}}{k_x^A}} \qquad b_y = \beta_y h_y = \sqrt{\frac{\mathsf{D}_{3232}}{k_y^A}} \tag{17}$$

3.4. Parameters for the non-linear response and damage

The assignment of reliable values to the shear strength and the elasticity modulus is somehow uncertain due to the fact that the experimental tests, at the macroscale, configure situations in which the stress is not homogeneous. For example, the practice often contamplates the diagonal compression tests for the identification of the shear response, but the detemination of the shear elastic modulus with this test is not so straightforward [54–56]. On the other hand, in situ shear-compression tests on masonry walls made by roughly cut stone blocks show a large variability, but above all this test can provide resistance values about twice those estimated with the diagonal compression, and also the shear elastic modulus is much higher [57].

In what follows, the basic rules assumed for the hysteretic response are described qualitatively. Overall, the main character of the adopted non-linear response of the axial and shear spring-bonds is a marked softening branch, and the micro-structure effects related to the masonry texture are obtained by assigning different characteristics to the vertical and horizontal springs [28]. Thus, the mechanical parameters of the spring-bonds are assigned at the macro-scale with the aim to accomplish three main characters of the post-elastic and hysteretic behaviour: (i) *Tension*: the tensile strength is very low, the response is brittle, and an early mechanical degradation is observed, with little energy dissipation under cyclic loading. The RBSM model allows to assign different properties along the material axes, to account for an horizontal tensile strength larger than the vertical one. (ii) *Compression*: in this case the material exhibits its maximum bearing capacity with a limited ductility, while a progressive mechanical degradation and energy dissipation is related to the progressive crushing, once the peak value of strength is reached. (iii) *Shear*: the spring-bonds accomplish for an orthotropic post-elastic response; the internal friction significantly enhances the shear strength of the horizontal shear spring-bond in the case of normal compression, while this effect is less relevant for the vertical shear joints. On the other hand, the initial strength of a vertical shear spring-bond should be larger at as a consequence of the interlocking between the masonry blocks. Energy dissipation, also in the case of repeated cycles of loading, is significant as a consequence of the internal friction [58].

These observations were condensed into the formulation of two types of constitutive behaviour for the axial and the shear bond springs, recalling here that a RBSM was also implemented by Fu et al. [59] to model the shear cracks in reinforced concrete by giving different hysteretic cycles to the axial and shear springs. The present hysteretic

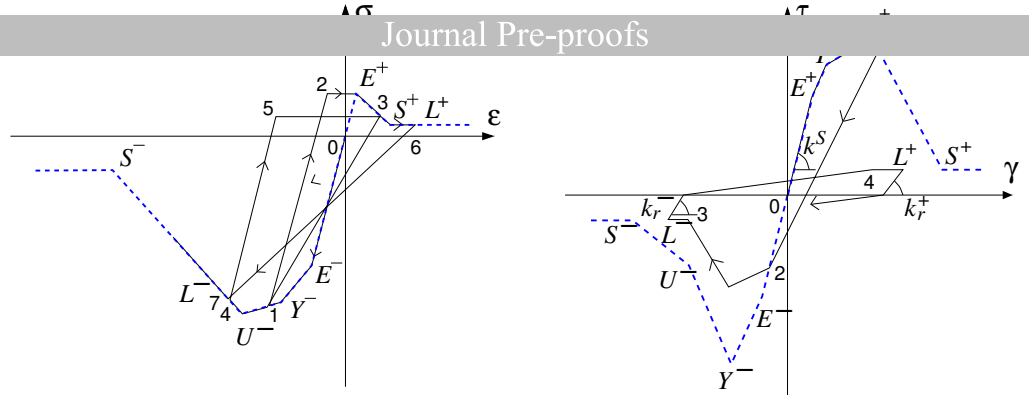

Figure 6: Hysteretic behaviour of the axial (left) and shear (right) connecting springs.

responses, inspired also by the Takeda constitutive model [60], are schematically shown in Fig. 6 by following the paths indicated by the sorted points 1-2-3-... [61]. The segment E^-0E^+ corresponds to the initial linear elastic behaviour of the spring-bond. The skeleton curves, indicated with the blue dashed lines, degrade depending on the maximum positive and maximum negative deformation reached during the loading history. Out-of the range of deformation defined by interval $[S^-, S^+]$, a residual strength remains constant until the ultimate deformation is reached. The degradation of loading stiffness, of unloading stiffness and of strength, depends on the maximum deformation reached. The points L^+ and L^- are important for establishing the state of each spring-bond. At the beginning of a loading history, these points coincide with points E^+ and E^-, respectively, and they delimit the initial elastic range, while in the plastic field they move along the skeleton curve, eventually degraded. Their abscissae correspond to the maximum positive deformation ε_L^+ (or γ_L^+ for a shear spring-bond) and the maximum negative deformation ε_L^- (or γ_L^-) reached by a spring-bond during the loading history. For the axial spring-bond subjected to compression, the loading stiffness is defined so that the actual stress-strain point (σ, ε), heads towards L^-. The same happens for the shear spring-bond, where the actual stress-strain point (τ, γ), heads towards L^- or L^+, but in this case there is also an isotropic degradation of the skeleton curve. During the unloading phase, the following degradation rule is assumed:

$$k_r^+ = k_E \left(\frac{\gamma_E^+}{\gamma_L^+}\right)^a \qquad , \qquad k_r^- = k_E \left(\frac{\gamma_E^-}{\gamma_L^-}\right)^a \tag{18}$$

In the present study, the exponent $a = 0.1667$ is assumed to obtain a small degradation of the unloading stiffness of the shear-bond, while $a = 0$ is given to the axial spring-bond.

In the case of inclined elements, the strength of the axial (and also shear) springs depends on the angle of orientation (α) of the corresponding edge, according to a linear

relationship, as follows:

$$\sigma_Y(\alpha) = \frac{2\alpha}{\pi}\left(\sigma_Y^v - \sigma_Y^h\right) + \sigma_Y^h \tag{19}$$

4. Material assumptions for the RBSM nonlinear analyses

The elastic moduli assigned to the masonry material are $E = 2800$ MPa and $G = 2333$ MPa, while the half of these values were given to the soil below the foundation area. The other material parameters assigned to define the mechanical response of the spring-bonds of the masonry materials are reported in Tables 2 and 3, where the letters E, Y, U, S make reference to the skeleton curves shown in Figure 6. These values have been selected with the aim to simulate the behaviour of an "average" masonry tower, well in the range of the most common parameters that can be found in the technical literature and regulations, by considering that usually masonry towers are made of good quality materials [1, 47, 49, 50, 62–69]. The values are expressed in terms of stress units (MPa) and strain, in order to make easier the comparison with the data that are commonly given in the technical literature, and they make reference to the specific average size of

Table 2: Material parameters given to the axial spring-bonds.

	horizontal		vertical	
	strain	stress	strain	stress
	‰	MPa	‰	MPa
E^-	-0.36	-1.00	-0.36	-1.00
Y^-	-1.00	-2.00	-1.00	-2.00
U^-	-2.00	-1.75	-2.00	-1.75
S^-	-4.00	-0.20	-4.00	-0.20
E^+	.072	0.20	.036	0.10
S^+	1.00	0.10	1.00	0.05

Table 3: Material parameters given to the shear spring-bonds.

	horizontal		vertical		symmetric	
	strain	stress	strain	stress	strain	stress
	‰	MPa	‰	MPa	‰	MPa
E	0.023	0.054	0.023	0.054	0.023	0.054
Y	0.070	0.088	0.050	0.088	0.060	0.088
U	0.107	0.097	0.187	0.165	0.147	0.131
S	0.600	0.010	1.049	0.010	0.825	0.010

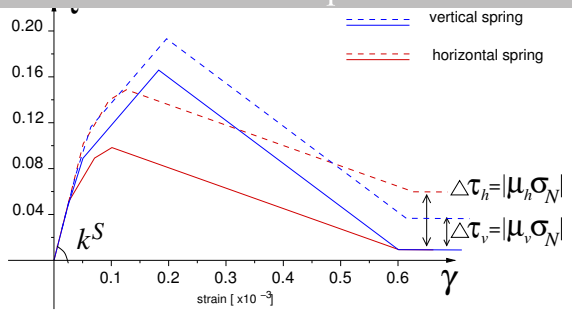

Figure 7: Variation of the skeleton curve for the shear spring-bond $\tau - \gamma$. σ_N is the compression normal to the shear spring.

the discrete elements of the stem of tower model (about 0.75 m $\times$ 1.05 m). The variability of these elements size is however minimal in the present model.

Clearly, the shear strength should depend also on the presence of a normal compression stress σ_N, due to the effect of internal friction coefficient, μ, which is different for the horizontal and vertical shear bondings. To this aim, the points that define the effective skeleton curve of the shear spring-bonds are translated by $\Delta\tau = -\mu\sigma_N \,\mathrm{sgn}(\tau)$ and $\Delta\gamma = \Delta\tau/k^S$ as sketched in Figure 7. The value attributed to the internal friction coefficient should be interpreted as a macroscopic parameter and should ideally account for the effects of meso-scale wall bonding-texture. An analysis of the values reported in the literature shows an high variability also in this case, and in particular the anisotropy of this effect has not been experimentally measured, yet. A numerical research on this aspect was done through a rather elementary finite element model, presented in [28], where it appeared quite clearly that the average shear strength increases linearly with a compression normal to the horizontal mortar joints, while there is a little sensitivity to the presence of a compression parallel to the horizontal mortar joints. For clarity, considering this as a stimulus for further investigations, both experimental and numerical, it was therefore decided to compare 2 simple options: i) a full orthotropic material with $\mu_h = 1.0$ and $\mu_v = 0.2$ for the horizontal and vertical shear springs; ii) a material with a symmetric shear response with $\mu_s = 0.6$, that is the average of the previous parameters. In the second case it was also assumed $\sigma_N = (\sigma_v + \sigma_v)/2$ in order to obtain a shear response close to the Drucker criterion. In the reality, these factors are quite dispersed in the case of historical tower walls and the data that could support a quantitatively plausible approach to a macro-scale analysis should also consider the compatibility with some reference values of the shear fracture energy [31, 33, 70, 71] which incorporate the size of the discrete elements adopted. In the present case, on the basis of the data reported in Table 3, and

making reference to the size of the quadrilateral elements adopted in the the central part of the mesh adopted for the numerical examples shown in the next section, the values of $G_h^{f\text{II}} = 0.016$ N/mm and $G_v^{f\text{II}} = 0.075$ N/mm are given. These values, which are given in correspondence of zero normal stress, are affected by the internal friction, coherently with the data reported in the Tables 2 and 3, and ultimately the actual shape of the shear hysteretic loops tends to resemble a rectangle whose height is essentially determined by the resistance due to the effect of internal friction [58, 72].

5. Numerical application

5.1. General characters of the tower model

The medieval masonry towers present a wide range of different slendernesses. Some, typically those used for defensive and military purposes, are stocky and stiff, with a prevailing shear deformation while the vertical compression load is low. In these cases the most probable cracking mechanism consists in the shear sliding of the horizontal mortar joints in the façade walls. On the other hand, the bell towers, often tall and slender, typically suffer due to excess of flexural bending at the base, while the higher modes of vibration can cause damages to the belfry. The most interesting cases have an intermediate behaviour, which is widespread in Italy, like the model proposed in this research. They may present different damage and craking mechanisms, both shear and flexural, sometimes combined with each other. The observation of the real towers, even if not directly affected by destructive seismic events, offers many hints to understand what could be the weakness of these buildings. For example, in the study on the Arcisate tower (Lombardia, Italy), the vertical cracks passing through the central area of the façade walls were much evident, as explained by Gentile and Saisi [73]: "Along all sides, the tower exhibits long vertical cracks, with most of them cutting the entire wall and passing through the keystones of the arch window openings. These cracks are mainly detected between the third floor order and the base of the belfry, and the maximum apertures generally correspond to the upper end".

An appropriate numerical model for this typology should therefore be able to show the possible activation of the different damages considering that a seismic ground motion is a dynamic combination of horizontal and vertical actions [68, 74]. As an example of this approach, the dynamic behaviour of a series of masonry towers was recently analyzed with a RBSM approach, attributing to the shear springs a limited difference in resistance

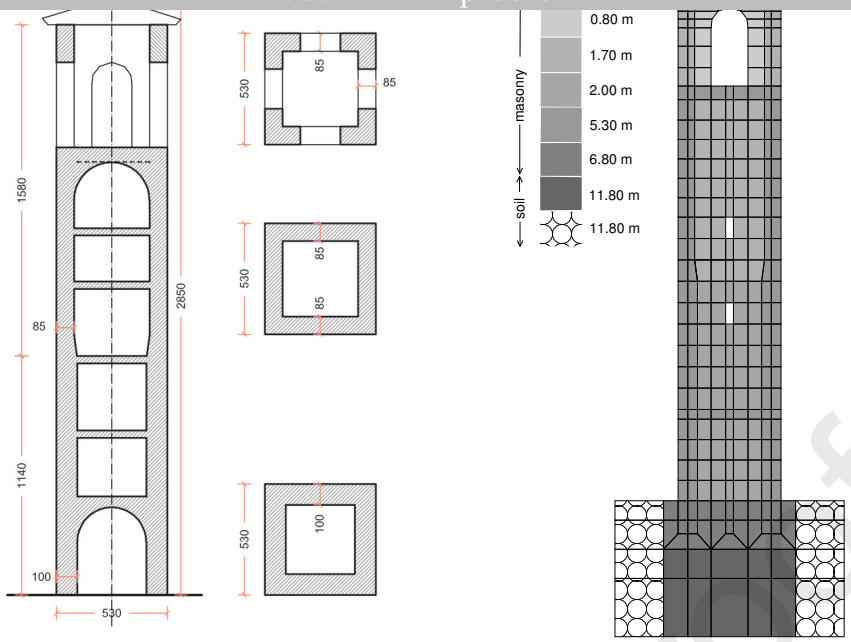

Figure 8: Schematic section and plan views of the idealized case study (on the left). Discrete model, materials and thickness (on the right).

[74]. The damage patterns that were obtained showed a good adherence to what would have been expected on the basis of the empirical experience, especially in relation to the different geometric typologies of the towers [66, 67, 75–77].

The novelty of present investigation is to focus the specific effect of the orthotropic shear strength model on the prediction of the overall damage pattern. The reference tower model has been supposed to be structurally independent, i.e. with no adjacent interacting construction, and characterized by geometrical regularity both in plan and in elevation (see Figure 8). The main geometrical data are reported in Table 4, while some minor details about the mesh can be found in [78]. The thickness of the masonry elements was defined in order to deal with a plane model of the tower in elevation, while the thickness of the elements below the foundation was assigned with the aim to obtain a reasonable participation mass of soil. A reduced modulus (1/10) was given to the horizontal axial springs and to the vertical shear springs of the two columns of elements of soil, indicated with the bubbles dithering, at the vertical boundary of the discrete model. This strategy was needed in order to obtain a good match of this simple plane model, of only 858 degrees of freedom, with the eigenvalue analysis of a much more refined three dimensional finite element model (with about 100.000 degrees of freedom) that was previously adopted to study the effects of the soil-foundation interaction to this reference tower [79]. It should be noted that the thickness of the façade walls is so large that no significant out-of plane

flexural damage was expected, as already confirmed by the cited three dimensional finite element model.

Table 4: Some geometric and global dynamical characteristics of the discrete model of reference tower.

Total height	28.50 m
Base	5.30 m × 5.30 m
Base wall thickness	1.00 m
Frequency 1^{st} mode	1.76 Hz
Frequency 2^{nd} mode	7.35 Hz

5.2. Monotonic lateral loading

A first series of numerical analyses was performed considering the tower subjected to the vertical gravity load combined with an increasing lateral load. The vertical forces were applied at first, slowly enough to avoid significant inertial effects, to all the elements of the model, up to the gravity value, which was then kept constant over time. Subsequently, the horizontal forces were applied, also proportional to the masses of the discrete elements and increasing according to a "S-shaped" time-history curve, until a value that triggers a collapse mechanism, and therefore they were kept constant until the full development of the corresponding kinematics. In order to enhance the numerical convergence and to obtain a behaviour similar to that of a quasi-static analysis, a viscous damping value equal to 99% of the critical damping was given to the first natural mode of vibration. The second mode was damped at 24% of the critic, in accordance with the typical behaviour of the Rayleigh damping, assuming a $[C]$ matrix proportional to the mass matrix. In any case, it was always verified that the resultant viscous force, measured at the base, remained very small and negligible when compared to the total reacting force applied at the base of the model.

In the Fig. 9, a synthesis of these analyses is reported to compare the symmetric versus no-symmetric shear spring responses. In these drawings, the points A_s (for the tower with symmetric shear springs) and A_n (no symmetric shear springs) indicate the time at which the data were extracted to report the maps of the deformation associated to the shear springs, and the displaced shape of the towers at the beginning of collapse.

From the comparison of these responses, it is noted that the model with symmetrical shear springs shows a capacity to withstand a higher lateral load, corresponding to a lateral

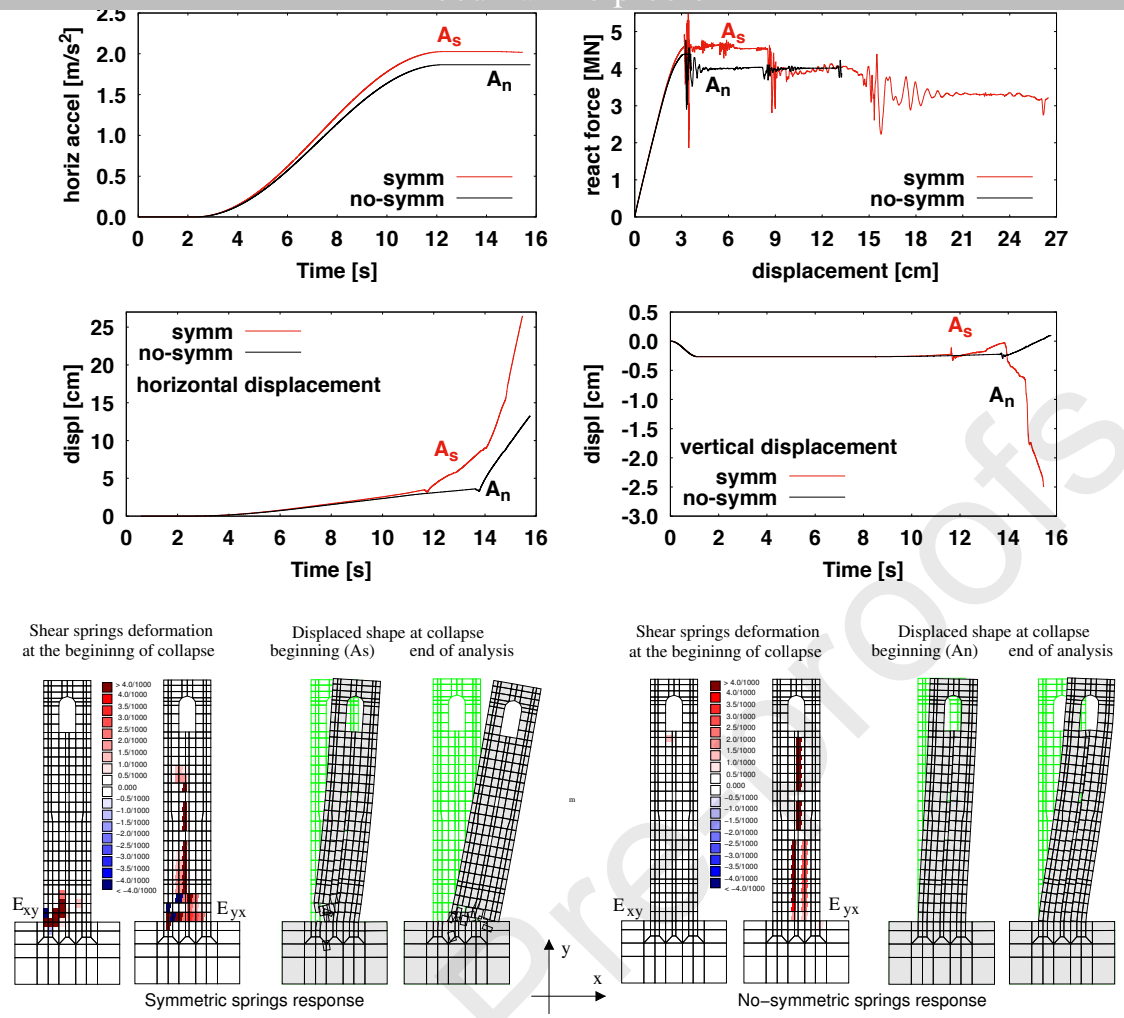

Figure 9: Comparisons of the response with the symmetric vs no-symmetric shear springs when subjected to increasing horizontal loading. Time histories, deformed spring maps, displaced shapes (much enlarged) at the beginning of collapse, indicated with points A_s and A_n, and final configuration at the end of the numerical analyses.

acceleration equal to 2.027 m/s ^{2} against the 1.866 m/s ^{2} for the case with no-symmetric springs. It is noticeable that the overall aspect of the response with the symmetric shear material is quite similar to what obtained by Preciado [69, 80] which considered a three dimensional model of isolated tower. The higher values of the reacting force in the present case just corresponds to the mass of the discrete ground elements considered below the foundation to account for the soil-structure interaction. The most interesting aspect, however, consists in observing the difference between the two collapse kinematics, that mainly consists in a mixed flexural and shearing deformation at the base of the tower in the model with symmetric shear springs, while in the case of no-symmetric springs the prevalent mechanism consists of vertical shear slidings that develop along the entire height of the tower. The final collapse in the first case leads to a crushing of the base section

Figure 10: Left: Bell tower of the main church in Gemona, after the Earthquake on May 1976. Centre: Clock tower in Finale Emilia after the Earthquake on May 2012. Right: detail of the damage to a bell tower in Sant'Agostino after the Emilia Earthquake on May 2012.

and subsequent rotation of the entire tower, while with the no-symmetric shear springs the cracks propagate according to a mode II, which develops along a vertical plane and affects the tower throughout its height. In this case, the tower tends to become separated, along the shaft, into two-pieces sliding along a system of vertical cracks. It is worth to compare this with the pictures shown in Fig. 10, that show the cases of three bell towers hit by some major earthquakes in Italy. From these images it appears that the pattern of shear damage obtained with no-symmetric shear springs is quite representative of the phenomenology of the damage pattern when it is dominated by the vertical shear cracks along the tower shaft.

5.3. The dynamic response: sym *versus* no-sym *shear springs*

The seismic response is the aspect that mainly concerns this type of structure, and therefore it is essential to examine their dynamic behaviour. The numerical model was then loaded by a set of different accelerogram pairs (horizontal and vertical component) recorded during various Italian earthquakes. The intensity of these strong motions is compatible with the provisions of the Italian regulations for the seismic areas in central Italy. The acceleration recordings that are indicated with the event code *FR2-76a*, *FR2-76b*, *FR2-76c*, in the Table 5, have been selected from the earthquake sequence recorded in Gemona (station GMN) during the Friuli (Italy) Earthquake in September 1976, while the event code *UMM-97b*, refers to the main shock recorded in Nocera (station NCR) during the Umbria-Marche (Italy) Earthquake on September 26, 1997.

Table 5: Selected strong ground motions [81–83].

Event name	Date / UTC time	Latitude	Longitude	M_L	M_W	Event code
Friuli 2^{nd} main	1976-09-11 / 16:35:01	46.30	13.32	5.8	5.6	*FR2-76a*
	1976-09-15 / 03:15:18	46.30	13.20	6.1	5.9	*FR2-76b*
	1976-09-15 / 09:21:18	46.30	13.18	6.0	6.0	*FR2-76c*
Umbria-Marche	1997-09-26 / 09:40:25	43.02	12.85	5.8	6.0	*UMM-97b*

In this section, the results of a reduced set of 8 pairs of responses is presented, which is representative of the most typical behaviours that were noticed. The main data of these recordings are reported in Table 6, where three parameters are provided in order to appreciate the destructive potential of the North-South (NS), West-East (WE) and vertical (UP) components of the ground motions. The peak ground acceleration (PGA) and velocity (PGV) are related to the ground motion intensity in the short periods and in the intermediate periods range of the response spectrum, respectively. The last three columns of Table 6 report the spectral intensity SI defined by Housner [84] as the integral of the pseudo-velocity response spectrum over the period range of [0.1 s − 2.5 s], and assuming a damping ratio of 5%. For completeness, the Fig. 11 shows the graphs of the corresponding response spectra in terms of acceleration.

The numerical results showed a considerable variability of the responses with regards to the level of damage, and also with regards the type of damage pattern. A graphical synthesis of these results is given in the Figures 12 - 19 with the aim to catch the differences between the two approaches chosen to model the shear behaviour. The intermediate characteristics of the tower model permitted to obtain various damage mechanisms for this type of structure, dipending on the different accelerograms. In general, the damage at the top, to the belfry, is often present, even in the cases of the less destructive ground

Table 6: Selected stations and recordings [81–83]. R_{epi} is the distance from epicentre, PGA the peak ground acceleration, PGV the peak ground velocity and SI is the spectral intensity defined by Housner [84].

Event code / Station	R_{epi}	PGA [cm/s^2]			PGV [cm/s]			SI [cm]		
	[km]	NS	WE	UP	NS	WE	UP	NS	WE	UP
FR2-76a / GMN	9.4	322	293	231	36.7	20.3	13.4	98.5	64.3	43.6
FR2-76b / GMN	6.2	318	636	476	34.0	68.5	20.7	140.3	232.2	67.7
FR2-76c / GMN	4.0	247	250	265	13.5	30.4	7.6	50.2	90.4	21.7
UMM-97b / NCR	10.9	492	415	398	32.6	28.7	21.2	74.4	80.3	56.2

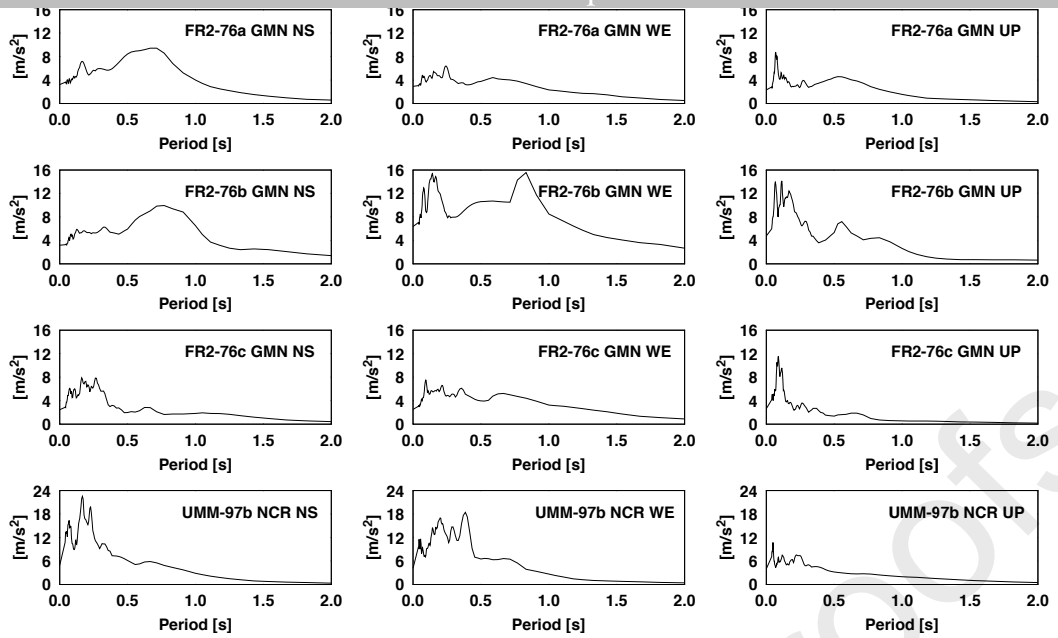

Figure 11: Acceleration response spettra of the selected strong motions.

motions. This damage can occur in different ways, sometimes with the shear crack of the bell chamber pillars, or due to the deflection of these pillars. The breakdown at the top of the arch window openings led also to the collapse of the covering of the belfry itself, in some other cases. The damages in the main façade of the tower were obtained by applying the most destructive strong ground motions, and consisted of 3 fundamental mechanisms: i) collapse due to bending at the base with the compression crushing of the most stressed part of the façade walls; ii) collapse due to a mixed mechanism of bending and shear with a rotation around the central part of the tower façade; iii) collapse triggered by the develop of vertical shear cracks along the entire height of the main façade walls.

The Figs. 12 - 19 show the time histories of the horizontal and vertical displacements obtained by averaging the values at two points that were selected just above the pillars supporting the arch window of the belfry. Furthermore, the maps of the residual deformation of the shear springs, at the end of the numerical analysis, are also shown. Both the shear residual deformation of the horizontal spring (E_{xy}) and that of the vertical spring (E_{yx}) are reported. These maps are usefull to distiguish the corresponding different distribution of the shear damage. Finally, the drawing of the deformed tower at the end of the numerical analysis, or just before the eventual collapse of the model, is shown. The displacement magnification factor for this latter picture is very high and was adapted for each image in order to maximize the graphical comprehensibility.

In detail, the Figs. 12 and 13 refer to the responses to the NS and WE component,

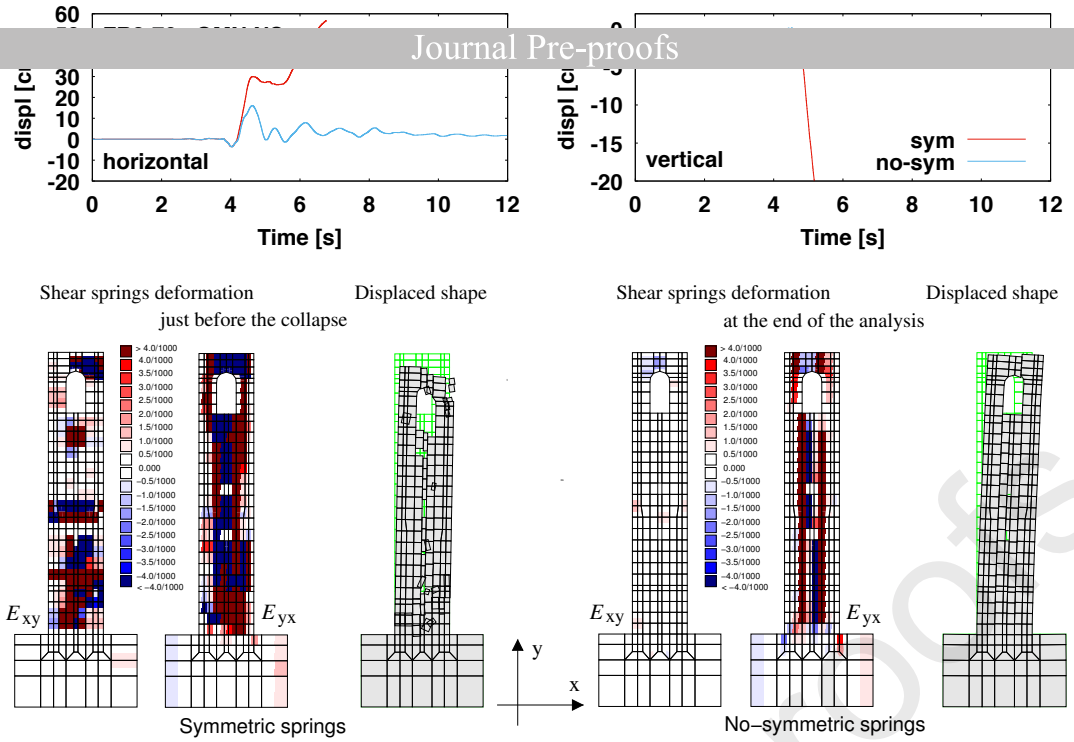

Figure 12: Numerical simulation with the Friuli Earthquake on September 11, 1976, recorded at Gemona, NS component. First row: displacement histories (average of two points at top). Second row: shear deformation and displaced map. Left side: model with symmetric shear springs just before the complete collapse. Right side: model with no-symmetric shear springs at the end of the numerical analysis.

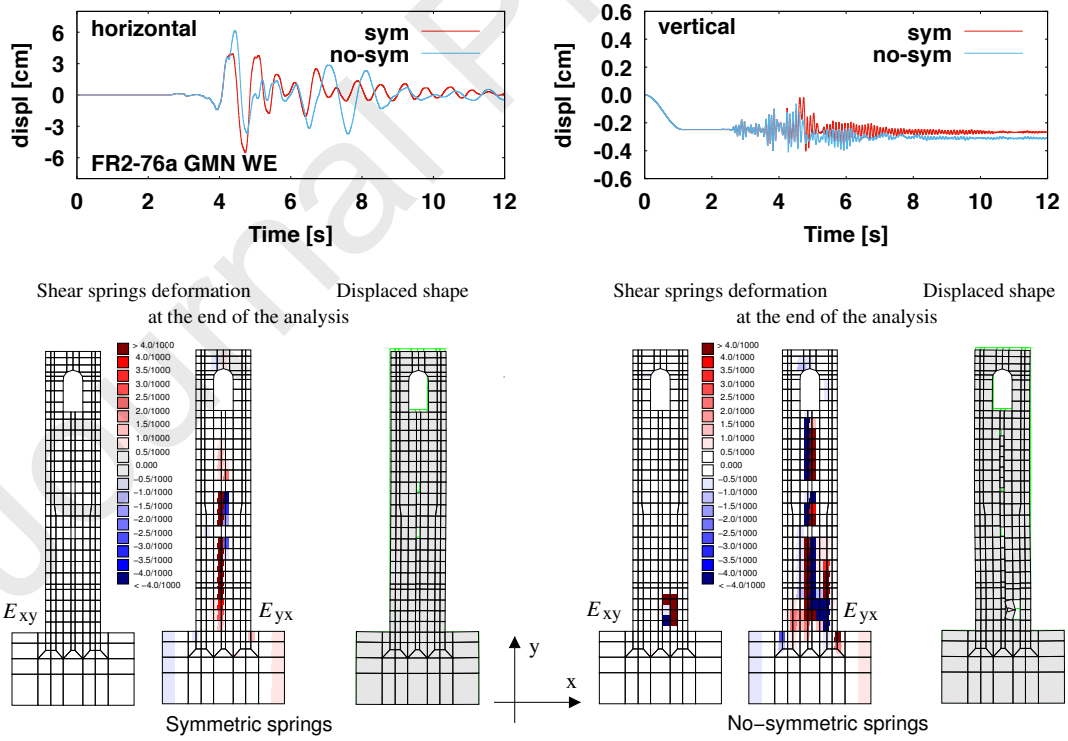

Figure 13: Numerical simulation with the Friuli Earthquake on September 11, 1976, recorded at Gemona, WE component. First row: displacement histories (average of two points at top). Second row: shear deformation and displaced map at the end of the numerical analysis. Left side: model with with symmetric shear springs. Right side: model with no symmetric shear springs.

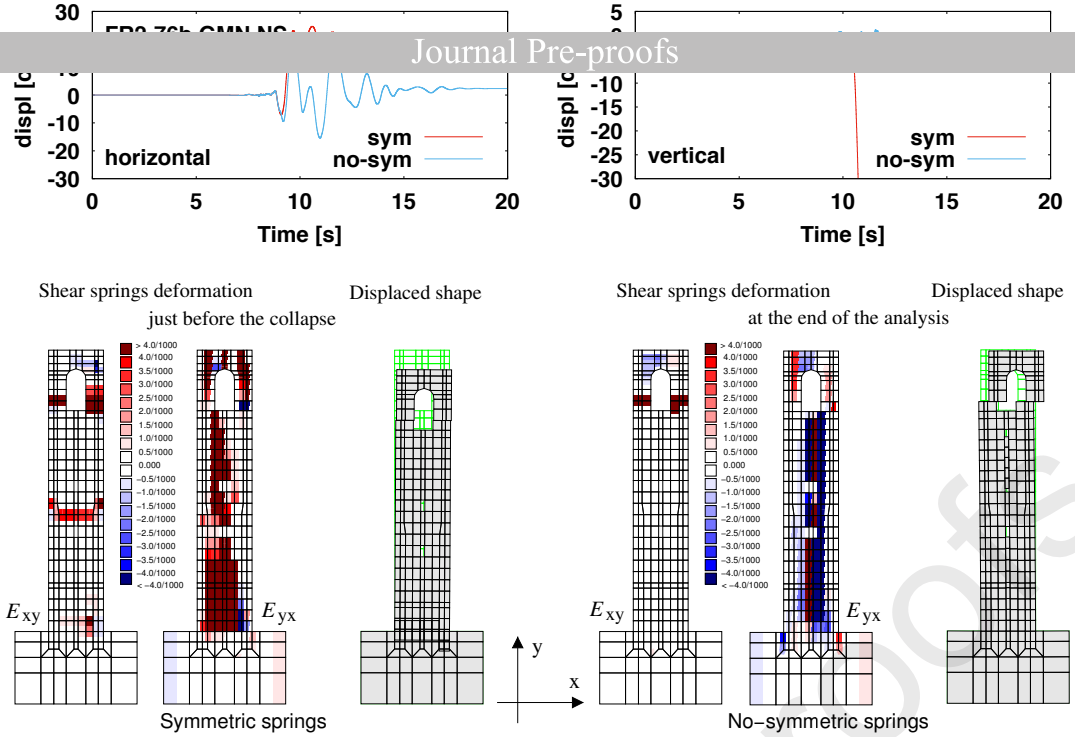

Figure 14: Numerical simulation with the Friuli Earthquake on September 15, 1976 (UTC 03:15:18), recorded at Gemona, NS component. First row: displacement histories (average of two points at top). Second row: shear deformation and displaced map. Left side: model with symmetric shear springs just before the complete collapse. Right side: model with no-symmetric shear springs at the end of the numerical analysis.

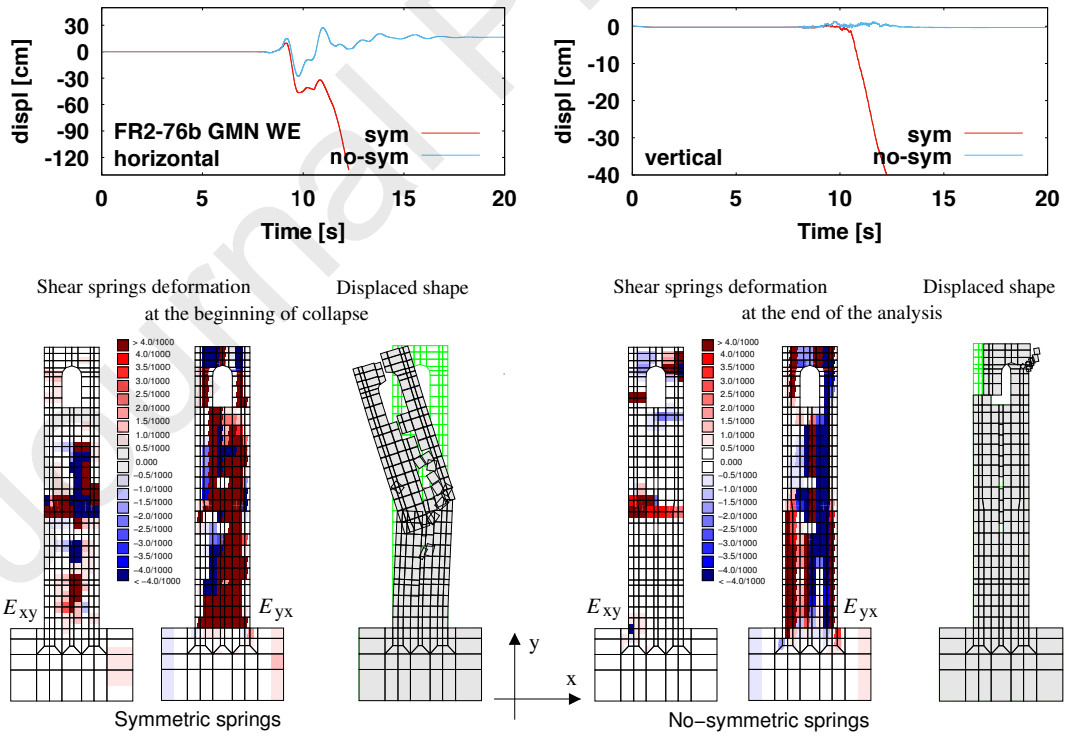

Figure 15: Numerical simulation with the Friuli Earthquake on September 15, 1976 (UTC 03:15:18), recorded at Gemona, WE component. First row: displacement histories (average of two points at top). Second row, shear deformation and displaced map. Left side: model with symmetric shear springs just before the complete collapse. Right side: model with no-symmetric shear springs at the end of the numerical analysis.

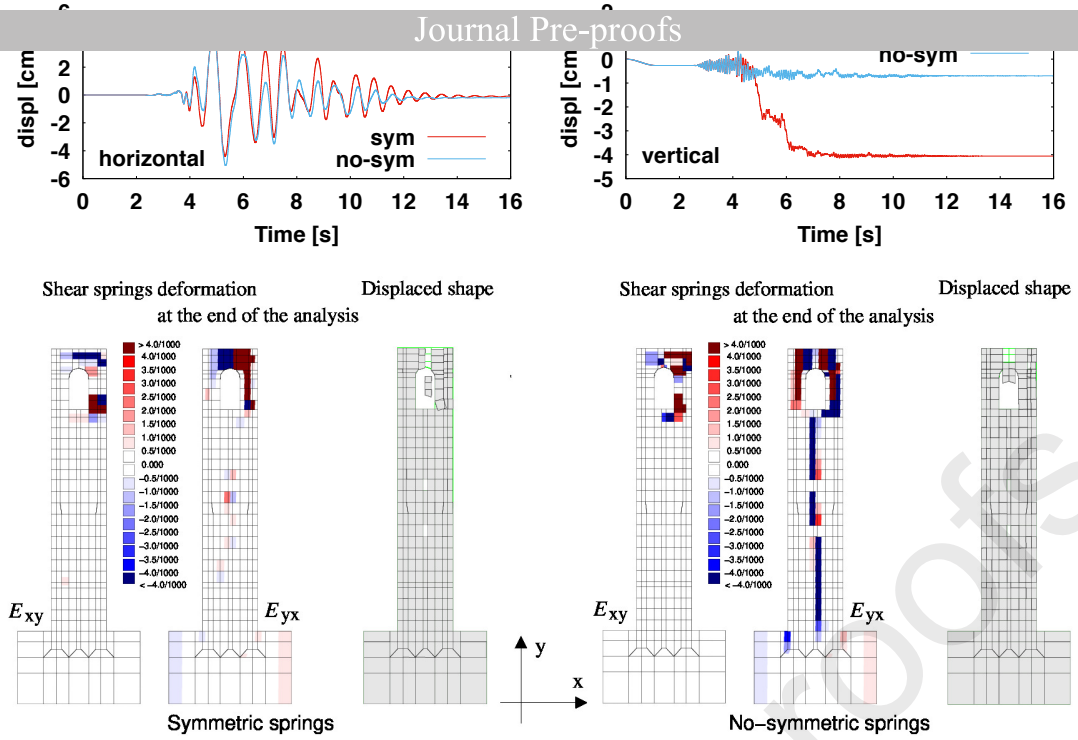

Figure 16: Numerical simulation with the Friuli Earthquake on September 15, 1976 (UTC 09:21:18), recorded at Gemona, NS component. First row: displacement histories (average of two points at top). Second row: shear deformation and displaced map at the end of the numerical analysis. Left side: model with with symmetric shear springs. Right side: model with no symmetric shear springs.

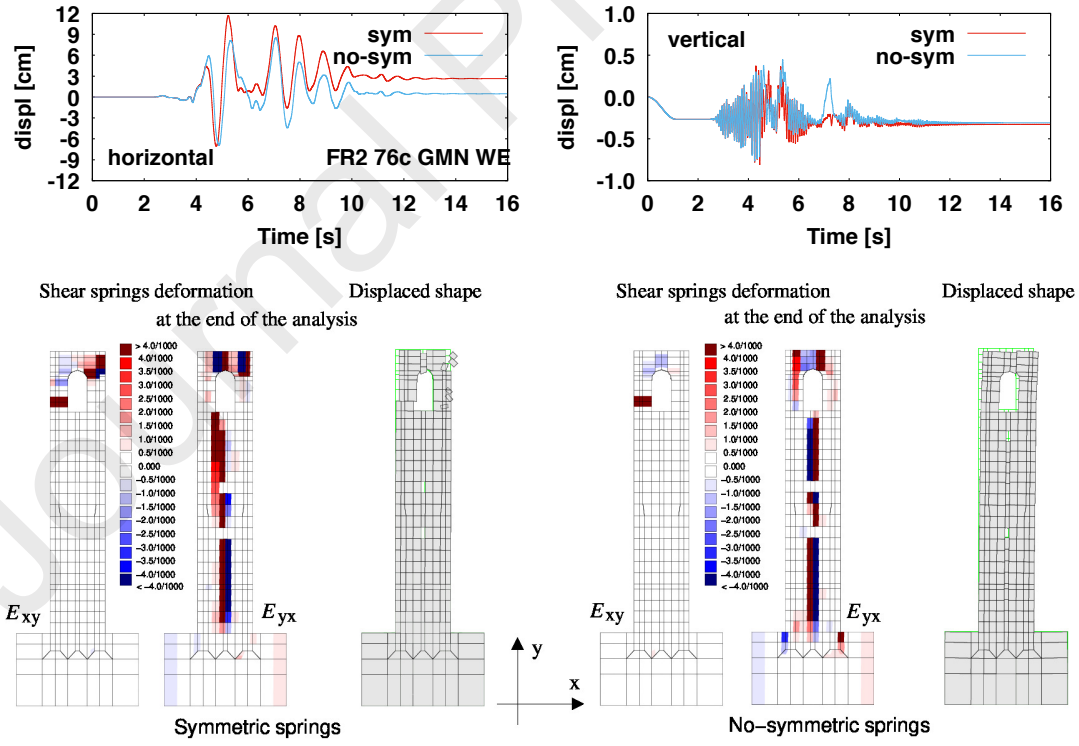

Figure 17: Numerical simulation with the Friuli Earthquake on September 15, 1976 (UTC 09:21:18), recorded at Gemona, WE component. First row: displacement histories (average of two points at top). Second row: shear deformation and displaced map at the end of the numerical analysis. Left side: model with with symmetric shear springs. Right side: model with no symmetric shear springs.

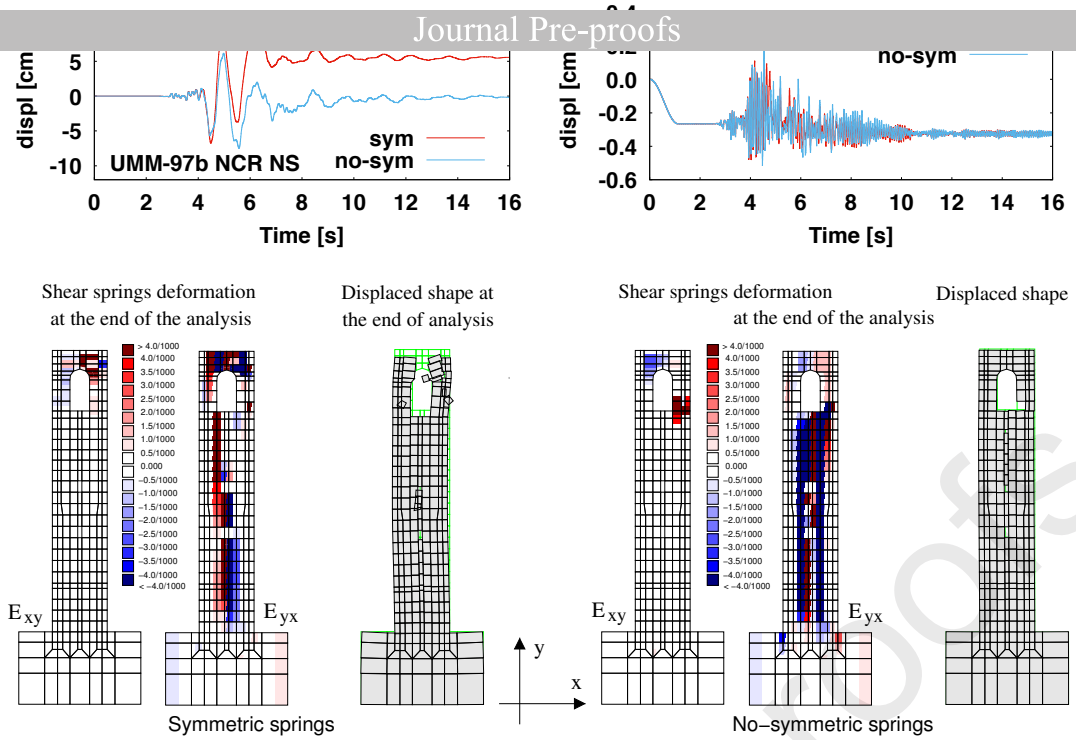

Figure 18: Numerical simulation with the Umbria-Marche Eqk on September 26, 1976, recorded at Nocera, NS component. First row: displacement histories (average of two points at top). Second row: shear deformation and displaced map at the end of the numerical analysis. Left side: model with with symmetric shear springs. Right side: model with no symmetric shear springs.

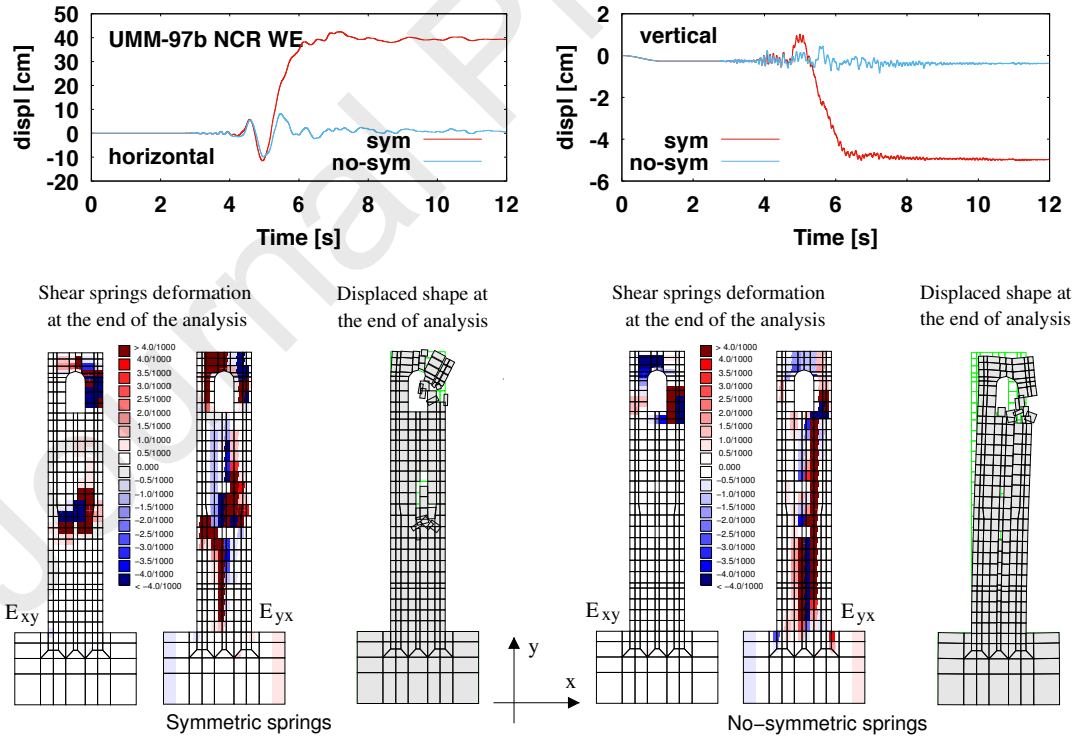

Figure 19: Numerical simulation with the Umbria-Marche Eqk on September 26, 1976, recorded at Nocera, WE component. First row: displacement histories (average of two points at top). Second row: shear deformation and displaced map at the end of the numerical analysis. Left side: model with with symmetric shear springs. Right side: model with no symmetric shear springs.

combined of with the UP component, of the event FR2-76a. With the NS component, in the case of symmetric shear springs, a numerical collapse occurred. The final kinematic mechanism was associated to an intense shear damage and sliding of the vertical springs along the whole façade which led to the subdivision of the tower into two parts, and finally to the crushing at the base for a combination of in-plane bending and compression. It should be noted that the symmetric shear model involved damaging the shear springs in the lower area of the tower, with shear sliding in the horizontal direction. The response of the model with no-symmetric shear springs to the same NS-UP pair appears very different, and did not lead to the collapse of the numerical model. In this case, the dynamic analysis was fully carried out with a maximum lateral displacements of about 15 cm. The map of the residual deformation of the shear springs at the end of this analysis shows a large residual sliding of the vertical springs, while the horizontal shear springs remained substantially within the elastic range. The map showing the shape of the model at the final step, shows that the residual deformation is essentially attributable to the shear damage. The Fig. 13 refers to the WE component of the same previous accelerogram, whose intensity is much lower. The comparison between the responses of the two shear models shows that the behaviour was quite similar, with the residual shear deformation that mainly involved the springs along the vertical direction. In this case, however, the model with no-symmetric springs shows a larger damage, with a first hint of damage at the base of the tower which seems to prelude to the complete separation of the tower into two vertical portions.

The Figs. 14 and 15 refer to the responses to the combination of the NS and WE component with the UP of the event FR2-76b which is characterized by a powerful spectrum in the medium-long periods (0.5 s – 1.0 s). This aspect, together with the fact that the recording is also very intense with regard to the vertical component, contributes to making this strong motion extremely dangerous to masonry towers. In fact, all these 4 numerical analyses report significant damages, with a global collapse in the case of the model with symmetric shear springs. These two global collapses appear quite different, since in the case of the NS horizontal component there was a disastrous crushing by compression at the base of the tower, with significant sliding for the vertical shear springs only. In the case of the WE component, the global collapse was more spectacular because it also involved the horizontal shear springs at mid-height of the shaft, with a more complex kinematics. On the other hand, in the case of the model with no-symmetric springs, it can be observed that the shear damage affected almost only the vertical springs and the

model, despite undergoing significant lateral displacements, reached the end of the time history with the only collapse of the belfry.

The Figures 16 and 17 refer to the event FR2-76c which is the least intense among those selected. In fact, the damage essentially concerned the belfry cell and there was not a global collapse mechanism in these numerical analysis, in any of the 4 combinations shown. The difference in response between the two shear models was quite small.

The last series of numerical analyses shown in Figures 18 and 19 refers to the combination of the NS and WE component with the UP of the event UMM-97b recorded during the 1997 Umbria-Marche earthquake. These recordings have an overall destructive potential similar to that of the first event, FR2-76a, selected for these analyses, however the spectral content in this case is shifted towards the shorter periods which tend to stress the higher natural modes of the tower. In fact, the damage pictures highlight the collapse of the belfry cell in all the 4 cases. The residual deformation of the vertical shear springs is prevalent with respect to the deformation of the horizontal shear springs, however a difference can be noted between the two models because in the case of symmetrical springs the damage was more relevant above the arch window of the belfry, while with the model of no-symmetric springs the small pillars that support the tower roof collapsed due to the shear actions.

6. Conclusions

The novelty of the present research consists in the comparison of two different masonry material models for the definition of the shear damage response. The dynamical analyses, in the context of a rigid body-spring model (RBSM) showed macroscopic diffences in the seismic responses of a model of masonry tower, an heritage building quite common in Italy and other Mediterranean countries.

The material that was defined as with "symmetric shear springs" provided an identical non-linear response for the shear springs along the horizontal and vertical direction, in accordance with an approach that substantially recalls the Drucker criterion. In this case, the increase in the elastic limit due to the effect of internal friction was a function of the average compression and did not make distinction between vertical and horizontal shear springs. This type of material damage, which is quite common in finite element modelling, is not always consistent with what is detected by field observations. In particular, finite element models based on isotropic material damage models tend to underestimate the damage due to shear sliding along vertical fractures.

The model defined as with "no-symmetric shear springs", on the other hand, assumed that the shear springs arranged along the vertical joints between the RBSM elements had a response which, in the absence of compression, had a higher strength, so as to simulate the interlocking due to the staggered joints between the blocks of the masonry [44]. However, the internal friction coefficient for vertical slidings is lower at the macroscale [28], and above all in this shear modelling the Coulomb friction effect depended only on the compression component orthogonal to the vertical fractures, which is almost null in masonry towers. This latter aspect makes the shear response distinctly different for the vertical and horizontal springs. Overall, it happened that the effect of internal friction tended to make the horizontal joints much more resistant at the base of the tower façade, while the shear resistance along the vertical joints changed little in the higher part. The author believes that this research shows how this type of modelling leads to more realistic results.

Further research should concern above all the set up of appropriate laboratory test methods to detect and measure the different response of masonry specimens subjected mainly to shear stresses that produce damage patterns according to the mode II cracks, along various orientation of the fractures. Moreover, the deepening of this study shall also explore in a parametric way the variability in the characteristics of the material and in the geometric typology.

References

[1] Orduña, A.. Non-linear static analysis of rigid block models for structural assessment of ancient masonry constructions. International Journal of Solids and Structures 2017;128:23 – 35. doi:10.1016/j.ijsolstr.2017.07.022.

[2] Petracca, M., Pelà, L., Rossi, R., Zaghi, S., Camata, G., Spacone, E.. Micro-scale continuous and discrete numerical models for nonlinear analysis of masonry shear walls. Construction and Building Materials 2017;149:296 – 314. doi:10.1016/j.conbuildmat.2017.05.130.

[3] Luciano, R., Sacco, E.. Homogenization technique and damage model for old masonry material. International Journal of Solids and Structures 1997;34(24):3191 – 3208. doi:10.1016/S0020-7683(96)00167-9.

[4] Gambarotta, L., Lagomarsino, S.. Damage models for the seismic response of

brick masonry shear walls. part ii: The continuum model and its applications. Earthquake Engineering and Structural Dynamics 1997;26(4):441–462. doi:10.1002/(SICI)1096-9845(199704)26:4<441::AID-EQE651>3.0.CO;2-0.

[5] Lourenço, P., de Borst, R., Rots, J.S.. A plane stress softening plasticity model for orthotropic materials. International Journal for Numerical Methods in Engineering 1997;(40):4033–4057.

[6] Addessi, D., Marfia, S., Sacco, E.. A plastic nonlocal damage model. Computer Methods in Applied Mechanics and Engineering 2002;191(13):1291 – 1310. doi:https://doi.org/10.1016/S0045-7825(01)00325-5.

[7] Uva, G., Salerno, G.. Towards a multiscale analysis of periodic masonry brickwork: A fem algorithm with damage and friction. International Journal of Solids and Structures 2006;43(13):3739 – 3769. doi:10.1016/j.ijsolstr.2005.10.004.

[8] Massart, T.J., Peerlings, R.H.J., Geers, M.G.D.. An enhanced multi-scale approach for masonry wall computations with localization of damage. International Journal for Numerical Methods in Engineering 2007;69(5):1022–1059. doi:10.1002/nme.1799.

[9] Lombardo, M., Zeman, J., Sejnoha, M., Falsone, G.. Stochastic modeling of chaotic masonry via mesostructural characterization. International Journal for Multiscale Computational Engineering 2009;7(2):171–185. doi:10.1615/IntJMultCompEng.v7.i2.70.

[10] Addessi, D., Gatta, C., Marfia, S., Sacco, E.. Multiscale analysis of in-plane masonry walls accounting for degradation and frictional effects. International Journal for Multiscale Computational Engineering 2020;18(2):159–180. doi:10.1615/IntJMultCompEng.2020031235.

[11] Cerrolaza, M., Sulem, J., Elbied, A.. A Cosserat non-linear finite element analysis software for blocky structures. Advances in Engineering Software 1999;30(1):69 – 83. doi:10.1016/S0965-9978(98)00059-3.

[12] Casolo, S.. Macroscopic modelling of structured materials: Relationship between orthotropic Cosserat continuum and rigid elements. International Journal of Solids and Structures 2006;43(3-4):475 – 496. doi:10.1016/j.ijsolstr.2005.03.037.

[13] Addessi, D., Sacco, E.. A multi-scale enriched model for the analysis of masonry panels. International Journal of Solids and Structures 2012;49(6):865 – 880. doi:10.1016/j.ijsolstr.2011.12.004.

[14] Forest, S., Barbe, F., Cailletaud, G.. Cosserat modelling of size effects in the mechanical behaviour of polycrystals and multi-phase materials. International Journal of Solids and Structures 2000;37(46):7105 – 7126. doi:10.1016/S0020-7683(99)00330-3.

[15] Bouyge, F., Jasiuk, I., Ostoja-Starzewski, M.. A micromechanically based couple–stress model of an elastic two-phase composite. International Journal of Solids and Structures 2001;38(10):1721 – 1735. doi:10.1016/S0020-7683(00)00132-3.

[16] Peerlings, R., Massart, T., Geers, M.. A thermodynamically motivated implicit gradient damage framework and its application to brick masonry cracking. Computer Methods in Applied Mechanics and Engineering 2004;193(30):3403 – 3417. doi:https://doi.org/10.1016/j.cma.2003.10.021.

[17] Ferrante, A., Loverdos, D., Clementi, F., Milani, G., Formisano, A., Lenci, S., et al. Discontinuous approaches for nonlinear dynamic analyses of an ancient masonry tower. Engineering Structures 2021;230:111626. doi:https://doi.org/10.1016/j.engstruct.2020.111626.

[18] Tavafi, E., Mohebkhah, A., Sarhosis, V.. Seismic behavior of the cube of zoroaster tower using the discrete element method. International Journal of Architectural Heritage 2021;15(8):1097–1112. doi:10.1080/15583058.2019.1650135.

[19] Ostoja-Starzewski, M.. Lattice models in micromechanics. Applied Mechanics Review ASME 2002;55(1):35–60. doi:10.1115/1.1432990.

[20] Casolo, S.. A linear-elastic heuristic-molecular modelling for plane isotropic micropolar and auxetic materials. International Journal of Solids and Structures 2021;224:111042. doi:https://doi.org/10.1016/j.ijsolstr.2021.111042.

[21] Griffiths, D.V., Mustoe, G.G.W.. Modelling of elastic continua using a grillage of structural elements based on discrete element concepts. International Journal for Numerical Methods in Engineering 2001;50(7):1759–1775. doi:10.1002/nme.99.

[22] Gerstle, W., Sau, N., Silling, S.. Peridynamic modeling of concrete structures. Nuclear Engineering and Design 2007;237(12):1250 – 1258. doi:10.1016/j.nucengdes.2006.10.002; 18th International Conference on Structural Mechanics in Nuclear Engineering.

[23] Cusatis, G., Pelessone, D., Mencarelli, A.. Lattice discrete particle model (LDPM) for failure behavior of concrete. i: Theory. Cement and Concrete Composites 2011;33(9):881 – 890. doi:10.1016/j.cemconcomp.2011.02.011.

[24] Ferretti, E.. The cell method: An enriched description of physics starting from the algebraic formulation. Computers, Materials and Continua 2013;36(1):49–71.

[25] Birck, G., Iturrioz, I., Lacidogna, G., Carpinteri, A.. Damage process in heterogeneous materials analyzed by a lattice model simulation. Engineering Failure Analysis 2016;70:157 – 176. doi:10.1016/j.engfailanal.2016.08.004.

[26] Casolo, S., Diana, V.. Modelling laminated glass beam failure via stochastic rigid body-spring model and bond-based peridynamics. Engineering Fracture Mechanics 2018;190:331–346. doi:10.1016/j.engfracmech.2017.12.028.

[27] Kawai, T.. New discrete models and their application to seismic response analysis of structures. Nuclear Engineering and Design 1978;48(1):207 – 229. doi:10.1016/0029-5493(78)90217-0; special Issue Structural Mechanics in Reactor Technology - Smirt-4.

[28] Casolo, S.. Macroscale modelling of microstructure damage evolution by a rigid body and spring model. Journal of Mechanics of Materials and Structures 2009;4(3):551–570. doi:10.2140/jomms.2009.4.551.

[29] Giuffré, A.. Protection of the architectural heritage against earthquakes; chap. A mechanical model for statics and dynamics of historical masonry buildings. No. 359 in CISM Courses and Lectures; Wien: Springer-Verlag; 1996,.

[30] Baraldi, D., Reccia, E., Cecchi, A.. In plane loaded masonry walls: Dem and fem/dem models. a critical review. Meccanica 2017;doi:10.1007/s11012-017-0704-3.

[31] Van Der Pluijm, R., Rutten, H., Ceelen, M.. Shear behaviour of bed joints. In: 12th International brick/block masonry conference. Madrid, Spain; 2000, p. 1849–1862.

[32] Senthivel, R., Lourenço, P.. Finite element modelling of deformation characteristics of historical stone masonry shear walls. Engineering Structures 2009;31(9):1930 – 1943. doi:10.1016/j.engstruct.2009.02.046.

[33] Augenti, N., Parisi, F.. Constitutive modelling of tuff masonry in direct shear. Construction and Building Materials 2011;25(4):1612 – 1620. doi:10.1016/j.conbuildmat.2010.10.002.

[34] Snozzi, L., Molinari, J.F.. A cohesive element model for mixed mode loading with frictional contact capability. International Journal for Numerical Methods in Engineering 2013;93(5):510–526. doi:10.1002/nme.4398.

[35] Syrmakezis, C.A., Asteris, P.G.. Masonry failure criterion under biaxial stress state. Journal of Materials in Civil Engineering 2001;13(1):58–64. doi:10.1061/(ASCE)0899-1561(2001)13:1(58).

[36] Lishak, V.I., Yagust, V.I., Yankelevsky, D.Z.. 2-d orthotropic failure criteria for masonry. Engineering Structures 2012;36:360 – 371. doi:10.1016/j.engstruct.2011.11.033.

[37] Shieh-Beygi, B., Pietruszczak, S.. Numerical analysis of structural masonry: mesoscale approach. Computers & Structures 2008;86(21):1958 – 1973. doi:10.1016/j.compstruc.2008.05.007.

[38] Pelá, L., Cervera, M., Roca, P.. An orthotropic damage model for the analysis of masonry structures. Construction and Building Materials 2013;41:957 – 967. doi:10.1016/j.conbuildmat.2012.07.014.

[39] O'Donnell, A.P., Kurama, Y.C., Taflanidis, A.A.. An analytical modeling framework for primary lateral-load-resisting unreinforced masonry walls. Earthquake Spectra 2016;32(1):367–392. doi:10.1193/092214EQS144M.

[40] Caddemi, S., Caliò, I., Cannizzaro, F., Pantò, B.. New frontiers on seismic modeling of masonry structures. Frontiers in Built Environment 2017;3:39. doi:10.3389/fbuil.2017.00039.

[41] Massart, T., Peerlings, R., Geers, M.. Mesoscopic modeling of failure and damage-induced anisotropy in brick masonry. European Journal of Mechanics - A/Solids 2004;23(5):719 – 735. doi:10.1016/j.euromechsol.2004.05.003.

[42] Małyszko, L.. In-plane shear and tensile strength tests of small brickwork specimens. In: Modena, L.R., editor. Proceeding of Structural Analysis of Historical Constructions. Padova, Italia; 2004, p. 291–298.

[43] Adams, D., Walrath, D.. Further development of the Iosipescu shear test method. Experimental Mechanics 1987;27(2):113–119. doi:10.1007/BF02319461.

[44] Casolo, S., Biolzi, L., Carvelli, V., Barbieri, G.. Testing masonry blockwork panels for orthotropic shear strength. Construction and Building Materials 2019;214:74 – 92. doi:https://doi.org/10.1016/j.conbuildmat.2019.04.116.

[45] Dhanasekar, M., Page, A., Kleeman, P.. The failure of brick masonry under biaxial stresses. In: Proceeding of the Institution of Civil Engineers; vol. 79. 1985, p. 295–313.

[46] Calderini, C., Cattari, S., Lagomarsino, S.. In-plane strength of unreinforced masonry piers. Earthquake Engineering & Structural Dynamics 2009;38(2):243–267. doi:10.1002/eqe.860.

[47] Atkinson, R.H., Amadei, B.P., Saeb, S., Sture, S.. Response of masonry bed joints in direct shear. Journal of Structural Engineering 1989;115(9):2276–2296. doi:10.1061/(ASCE)0733-9445(1989)115:9(2276).

[48] Lourenço, P.B.. An anisotropic macro-model for masonry plates and shells: implementation and validation. Tech. Rep. Rep. No. 03.21.1.3.07; Univ. of Delft, Delft, Holland and Univ. of Minho, Guimarães, Portugal; 1997.

[49] Vasconcelos, G., Lourenço, P.. Experimental characterization of stone masonry in shear and compression. Construction and Building Materials 2009;23(11):3337–3345. doi:10.1016/j.conbuildmat.2009.06.045.

[50] Vasconcelos, G., Lourenço, P.. In-plane experimental behavior of stone masonry walls under cyclic loading. Journal of Structural Engineering 2009;135(10):1269–1277. doi:10.1061/(ASCE)ST.1943-541X.0000053.

[51] Goldstein, H.. Classical mechanics. Addison-Wesley; 1953.

[52] Zienkiewicz, O., Taylor, R.. The Finite Element Method; vol. 2. London: McGraw-Hill; 1991.

[53] Casolo, S.. Modelling in-plane micro-structure of masonry walls by rigid elements. International Journal of Solids and Structures 2004;41(13):3625–3641. doi:10.1016/j.ijsolstr.2004.02.002.

[54] Brignola, A., Frumento, S., Lagomarsino, S., Podestà, S.. Identification of shear parameters of masonry panels through the in-situ diagonal compression test. International Journal of Architectural Heritage 2008;3(1):52–73. doi:10.1080/15583050802138634.

[55] Andreini, M., De Falco, A., Giresini, L., Sassu, M.. Mechanical characterization of masonry walls with chaotic texture: Procedures and results of in-situ tests. International Journal of Architectural Heritage 2014;8(3):376–407. doi:10.1080/15583058.2013.826302.

[56] Borri, A., Castori, G., Corradi, M.. Determination of shear strength of masonry panels through different tests. International Journal of Architectural Heritage 2015;9(8):913–927. doi:10.1080/15583058.2013.804607; cited By 2.

[57] Corradi, M., Borri, A., Vignoli, A.. Experimental study on the determination of strength of masonry walls. Construction and Building Materials 2003;17(5):325–337. doi:10.1016/S0950-0618(03)00007-2.

[58] D'Altri, A., Messali, F., Rots, J., Castellazzi, G., de Miranda, S.. A damaging block-based model for the analysis of the cyclic behaviour of full-scale masonry structures. Engineering Fracture Mechanics 2019;209:423–448. doi:10.1016/j.engfracmech.2018.11.046.

[59] Fu, L., Nakamura, H., Furuhashi, H., Yamamoto, Y., Miura, T.. Mechanism of shear strength degradation of a reinforced concrete column subjected to cyclic loading. Structural Concrete 2017;18(1):177–188. doi:10.1002/suco.201600052.

[60] Takeda, T., Sozen, M., Nielson, N.. Reinforced concrete response to simulated earthquakes. ASCE Journal of the Structural Division 1970;96(12):2557–2573.

[61] Casolo, S., Peña, F.. Rigid element model for in-plane dynamics of masonry walls considering hysteretic behaviour and damage. Earthquake Engineering & Structural Dynamics 2007;36(8):1029–1048. doi:10.1002/eqe.670.

[62] Ministero delle Infrastrutture e dei Trasporti, . Circolare n. 617. Istruzioni per l'applicazione delle "Nuove norme tecniche per le costruzioni" di cui al D.M. 14-01-2008; Gazzetta Ufficiale n. 47, Suppl. Ordinario n. 27 ed.; 2009.

[63] Carpinteri, A., Invernizzi, S., Lacidogna, G.. In situ damage assessment and nonlinear modelling of a historical masonry tower. Engineering Structures 2005;27(3):387–395. doi:10.1016/j.engstruct.2004.11.001.

[64] Bartoli, G., Betti, M., Giordano, S.. In situ static and dynamic investigations on the "torre grossa" masonry tower. Engineering Structures 2013;52:718 – 733. doi:10.1016/j.engstruct.2013.01.030.

[65] Acito, M., Bocciarelli, M., Chesi, C., Milani, G.. Collapse of the clock tower in Finale Emilia after the may 2012 Emilia Romagna earthquake sequence: Numerical insight. Engineering Structures 2014;72:70 – 91. doi:10.1016/j.engstruct.2014.04.026.

[66] Valente, M., Milani, G.. Non-linear dynamic and static analyses on eight historical masonry towers in the North-East of Italy. Engineering Structures 2016;114:241 – 270. doi:10.1016/j.engstruct.2016.02.004.

[67] Marra, A., Salvatori, L., Spinelli, P., Bartoli, G.. Incremental dynamic and nonlinear static analyses for seismic assessment of medieval masonry towers. Journal of Performance of Constructed Facilities 2017;31(4). doi:10.1061/(ASCE)CF.1943-5509.0001022.

[68] Sarhosis, V., Milani, G., Formisano, A., Fabbrocino, F.. Evaluation of different approaches for the estimation of the seismic vulnerability of masonry towers. Bulletin of Earthquake Engineering 2018;16(3):1511–1545. doi:10.1007/s10518-017-0258-8.

[69] Preciado, A., Sperbeck, S.. Failure analysis and performance of compact and slender carved stone walls under compression and seismic loading by the fem approach. Engineering Failure Analysis 2019;96:508–524. doi:10.1016/j.engfailanal.2018.11.009.

[70] Angelillo, M., Lourenço, P.B., Milani, G.. Masonry behaviour and modelling. Vienna: Springer Vienna. ISBN 978-3-7091-1774-3; 2014, p. 1–26. doi:10.1007/978-3-7091-1774-3_1.

[71] Wilding, B.V., Dolatshahi, K.M., Beyer, K.. Shear-compression tests of URM walls: Various setups and their influence on experimental results. Engineering Structures 2018;156:472 – 479. doi:https://doi.org/10.1016/j.engstruct.2017.11.057.

[72] Smoljanović, H., Nikolić, Z., Živaljić, N.. A combined finite-discrete numerical model for analysis of masonry structures. Engineering Fracture Mechanics 2015;136:1–14. doi:10.1016/j.engfracmech.2015.02.006.

[73] Gentile, C., Saisi, A.. Operational modal testing of historic structures at different levels of excitation. Construction and Building Materials 2013;48:1273 – 1285. doi:https://doi.org/10.1016/j.conbuildmat.2013.01.013.

[74] Casolo, S., Milani, G., Uva, G., Alessandri, C.. Comparative seismic vulnerability analysis on ten masonry towers in the coastal po valley in italy. Engineering Structures 2013;49:465 – 490. doi:http://dx.doi.org/10.1016/j.engstruct.2012.11.033.

[75] Doglioni, F., Moretti, A., Petrini, V.. Le Chiese e il Terremoto. Trieste: Lint press; 1994. In Italian.

[76] Bartoli, G., Betti, M., Vignoli, A.. A numerical study on seismic risk assessment of historic masonry towers: a case study in san gimignano. Bulletin of Earthquake Engineering 2016;14(6):1475–1518. doi:10.1007/s10518-016-9892-9.

[77] Ivorra, S., Pallarés, F.J.. Dynamic investigations on a masonry bell tower. Engineering Structures 2006;28(5):660 – 667. doi:https://doi.org/10.1016/j.engstruct.2005.09.019.

[78] Casolo, S., Uva, G.. Non-linear dynamic analysis of masonry towers under natural accelerograms accounting for soil-structure interaction. In: 4^{th}ECCOMAS, Thematic Conference on Computational Methods in Structural Dynamics and Earthquake Engineering. Crete, Greece; 2013, p. 4488–4506.

[79] Casolo, S., Diana, V., Uva, G.. Influence of soil deformability on the seismic response of a masonry tower. Bulletin of Earthquake Engineering 2017;15(5):1991–2014. doi:10.1007/s10518-016-0061-y.

[80] Preciado, A.. Seismic vulnerability and failure modes simulation of ancient masonry towers by validated virtual finite element models. Engineering Failure Analysis 2015;57:72–87. doi:10.1016/j.engfailanal.2015.07.030p.

[81] ITACA-Working-Group, . Data Base of the Italian strong motion records. 2020. http://itaca.mi.ingv.it.

[82] Luzi, L., Hailemikael, S., Bindi, D., Pacor, F., Mele, F., Sabetta, F.. Itaca (italian accelerometric archive): A web portal for the dissemination of italian strong-motion data. Seismological Research Letters 2008;79(5):716–722. doi:10.1785/gssrl.79.5.716. arXiv:http://srl.geoscienceworld.org/content/79/5/716.full.pdf+html.

[83] Pacor, F., Paolucci, R., Luzi, L., Sabetta, F., Spinelli, A., Gorini, A., et al. Overview of the italian strong motion database itaca 1.0. Bulletin of Earthquake Engineering 2011;9:1723–1739. Doi: 10.1007/s10518-011-9327-6.

[84] Housner, G.. Earthquake Engineering; chap. : Strong ground motion. Prentice-Hall; 1970, p. 75–91.